JCB Journal of Cell Biology

TOOLS

A fluorogenic complementation tool kit for interrogating lipid droplet–organelle interaction

Xiao Li[1*], Rico Gamuyao[1*], Ming-Lun Wu[1], Woo Jung Cho[2], Sharon V. King[3], R.A. Petersen[3], Daniel R. Stabley[3], Caleb Lindow[1], Leslie K. Climer[1], Abbas Shirinifard[3], Francesca Ferrara[4], Robert E. Throm[4], Camenzind G. Robinson[2], Yiwang Zhou[5], Alexandre F. Carisey[1], Alison G. Tebo[6], and Chi-Lun Chang[1]

Contact sites between lipid droplets and other organelles are essential for cellular lipid and energy homeostasis upon metabolic demands. Detection of these contact sites at the nanometer scale over time in living cells is challenging. We developed a tool kit for detecting contact sites based on fluorogen-activated bimolecular complementation at CONtact sites, FABCON, using a reversible, low-affinity split fluorescent protein, splitFAST. FABCON labels contact sites with minimal perturbation to organelle interaction. Via FABCON, we quantitatively demonstrated that endoplasmic reticulum (ER)- and mitochondria (mito)-lipid droplet contact sites are dynamic foci in distinct metabolic conditions, such as during lipid droplet biogenesis and consumption. An automated analysis pipeline further classified individual contact sites into distinct subgroups based on size, likely reflecting differential regulation and function. Moreover, FABCON is generalizable to visualize a repertoire of organelle contact sites including ER-mito. Altogether, FABCON reveals insights into the dynamic regulation of lipid droplet–organelle contact sites and generates new hypotheses for further mechanistical interrogation during metabolic regulation.

Introduction

Fatty acids are vital biomolecules; they are high-energy fuels for ATP production, building blocks for cell membranes, and signaling molecules for myriad biological functions. To harness such crucial molecules, eukaryotic cells develop an intricate interorganelle network to dynamically stockpile and consume fatty acids upon demand. Lipid droplets are the center of this network and interact with many other organelles at contact sites to coordinate fatty acid metabolism (Henne et al., 2018; Olzmann and Carvalho, 2019; Walther et al., 2017). Contact sites are an evolutionarily conserved form of nanoscale spatial organization where two heterologous organelles are dynamically tethered to form close appositions with a gap distance of ∼20 nm (Gatta and Levine, 2017; Prinz et al., 2020; Scorrano et al., 2019). This nanoarchitecture exists between virtually all organelles to facilitate efficient and direct material transfer. Endoplasmic reticulum–lipid droplet (ER-LD) contact sites are essential for fatty acid storage within lipid droplets, while mitochondria–lipid droplet (mito-LD) contact sites are associated with fatty acid consumption and energy production upon nutrient deprivation (Renne and Hariri, 2021). Contact sites between peroxisomes and lipid droplets (PX-LD) have been shown to facilitate the elimination of lipid peroxides and maintain energy homeostasis during fasting (Binns et al., 2006; Chang et al., 2019; Kong et al., 2020). Ultimately, lipid droplet–organelle contact sites have diverse yet interrelated roles in fatty acid metabolism. Defects in lipid droplet–organelle interaction are associated with many metabolic disorders and neurological diseases, such as hereditary spastic paraplegia, ataxia, and early-onset Parkinson's disease (Herker et al., 2021).

Despite their importance and recent research endeavors, the dynamic regulation of lipid droplet–organelle contact sites remains poorly understood primarily due to technical challenges that arise when detecting these nanoscale foci. Light microscopy (LM) in conjunction with colocalization analysis between fluorescently labeled organelles is currently the most common method for indirect, collective readout when assessing organelle interactions within a cell. This LM-colocalization pipeline is easy to implement and allows the acquisition of statistically

[1]Department of Cell and Molecular Biology, St. Jude Children's Research Hospital, Memphis, TN, USA; [2]Cell and Tissue Imaging Center, St. Jude Children's Research Hospital, Memphis, TN, USA; [3]Department of Developmental Neurobiology, St. Jude Children's Research Hospital, Memphis, TN, USA; [4]Vector Production and Development Laboratory, St. Jude Children's Research Hospital, Memphis, TN, USA; [5]Department of Biostatistics, St. Jude Children's Research Hospital, Memphis, TN, USA; [6]Janelia Research Campus, Howard Hughes Medical Institute, Ashburn, VA, USA.

*X. Li and R. Gamuyao contributed equally to this paper. Correspondence to Chi-Lun Chang: chi-lun.chang@stjude.org.

meaningful data across multiple temporal scales (Valm et al., 2017). However, the spatial resolution of LM is insufficient for the direct measurement of individual contact sites at the nanoscale, further hindering the investigation of questions involved in how contact sites are dynamically distributed throughout a cell over time. In addition, the application of LM colocalization is often restricted to flat, adherent model cell lines, preventing our understanding of contact site biology in physiologically relevant cellular systems.

Assays based on enhanced signal upon proximity, such as bimolecular fluorescence complementation (BiFC), have been developed to detect contact sites via LM (Alford et al., 2012; Cieri et al., 2018; Eisenberg-Bord et al., 2016; Harmon et al., 2017; Kakimoto et al., 2018; Shai et al., 2018). The BiFC method requires protein–protein interaction of cognate split fluorescent proteins (FPs) localized on heterologous organelles at membrane juxtapositions, which allows it to faithfully report the location of contact sites. This design enables the BiFC method to be readily applicable to detect any organelle contact sites of interest. However, the implementation of BiFC assays often relies on traditional split FPs, which causes issues such as irreversible complementation and fluorescence leakiness without cognate partners. These issues may interfere with contact site dynamics and result in high background fluorescence, respectively (Bishop et al., 2019; Romei and Boxer, 2019; Tashiro et al., 2020).

We reasoned that a reversible BiFC reporter could eliminate the inherent issues associated with traditional split FPs and thus significantly improve its ability to detect dynamic organelle interaction. A newly developed split FP system, splitFAST, appears to fit this purpose. This split system was engineered from the fluorescence-activating and absorption shifting tag (FAST), a 14-kDa apo-reporter that reversibly binds to hydroxybenzylidene rhodanine (HBR) analogs to become fluorescent (Plamont et al., 2016; Rakotoarison et al., 2024; Tebo and Gautier, 2019). HBR analogs are fluorogenic agents that strongly fluoresce when bound to splitFAST but are only weakly fluorescent in solution. The reversibility and high contrast signal from binding to HBR analogs make splitFAST an ideal reporter to implement BiFC when visualizing organelle contact sites with high spatial precision in living cells.

Here, we engineered and implemented the next-generation BiFC tool kit for quantitative visualization of lipid droplet–organelle contact sites using splitFAST. We named this tool kit FABCON, for Fluorogen-Activated BiFC at CONtact sites. We designed, generated, and validated a synthetic lipid droplet targeting motif based on Spastin's lipid droplet targeting hairpin (Hp) (Chang et al., 2019). This synthetic Hp motif is highly enriched on lipid droplets and minimally affects lipid droplets' functions. Next, we validated that splitFAST of low self-complementation ($splitFAST_{low}$) (Rakotoarison et al., 2024) is suitable for implementing FABCON, as it did not affect organelle interaction. We confirmed that FABCON is completely reversible with no detectable fluorescence leakiness within living cells. Through the lens of FABCON, most lipid droplets are capable of making contact sites with the ER and mitochondria. Both ER-LD and mito-LD contact sites appear to be dynamic domains on lipid droplets' surface and respond to distinct metabolic stimuli. While ER-LD contact sites were transiently increased during lipid droplet biogenesis, mito-LD contact sites were differentially and dynamically regulated during lipolysis and after inhibition of glycolysis. Via an automated line scanning algorithm, we quantitatively demonstrated the distinct sizes of individual ER-LD and mito-LD contact sites. Furthermore, FABCON is generalizable to visualize intermittent PX-LD contact sites and frequent ER-mito interaction. Altogether, our data demonstrate that, with proper organelle targeting and affinity, FABCON is an effective tool kit that can be used to uncover the dynamic regulation of lipid droplet-organelle interaction and beyond.

Results

Key factors for implementing FABCON

With the intention to visualize ER-LD, mito-LD, PX-LD, and other contact sites in living cells (Fig. 1 A), we designed a BiFC tool kit, FABCON, via fluorogen-activated splitFAST complementation (Fig. 1 B). We identified key factors for implementing FABCON that will allow us to dynamically visualize organelle contact sites in their native state. These factors are as follows: (i) the targeting mechanisms for localizing splitFAST to lipid droplets and other organelles and (ii) the affinity of splitFAST self-complementation to minimally affect organelle dynamics and proximity (Fig. 1 B). We experimentally addressed these issues in this work.

Engineering a synthetic lipid droplet–targeting motif

We first engineered a synthetic lipid droplet-targeting motif to localize splitFAST onto these organelles. Our previous study showed that M1 Spastin's Hp motif (1xHp, amino acid 43–92) has an affinity for lipid droplets (Chang et al., 2019). When overexpressed inside cells, this 1xHp motif was indiscriminately distributed between the ER and lipid droplets as detected by confocal microscopy in HeLa cells (Fig. 2, A and B) and by lipid droplet flotation assays of cell lysates from HepG2 hepatocytes (Fig. 2 D). This dual organelle distribution of the 1xHp motif hampered selective lipid droplet targeting. We reasoned that oligomerization of the Hp motif could increase its lipid droplet affinity (Chang et al., 2019), so we generated 6× tandem repeats of Hp (6xHp). In contrast to 1xHp, 6xHp was primarily distributed in lipid droplets with relatively low ER localization (Fig. 2, A–C). Moreover, 6xHp was highly enriched in lipid droplet fraction detected by flotation assays as compared with 1xHp (Fig. 2, E and F). The higher affinity of 6xHp was further demonstrated by fluorescence recovery after photobleaching (FRAP) analysis on large lipid droplets in U2OS cells. A moderate recovery was detected for the fluorescence of 1xHp because it can diffuse between the ER and lipid droplets. In contrast, only minimal recovery for the 6xHp fluorescence was observed following photobleaching (Fig. 2, G–I), suggesting that 6xHp was primarily static on lipid droplets' membrane. Furthermore, structured illumination microscopy with a twofold increase in resolution (Gustafsson, 2000) revealed that 6xHp localized to lipid droplets rather than to nearby ER membranes labeled with mEmerald-Sec61β (Fig. 2 J), supporting the idea that 6xHp directly localizes to the lipid droplet membrane monolayer. To

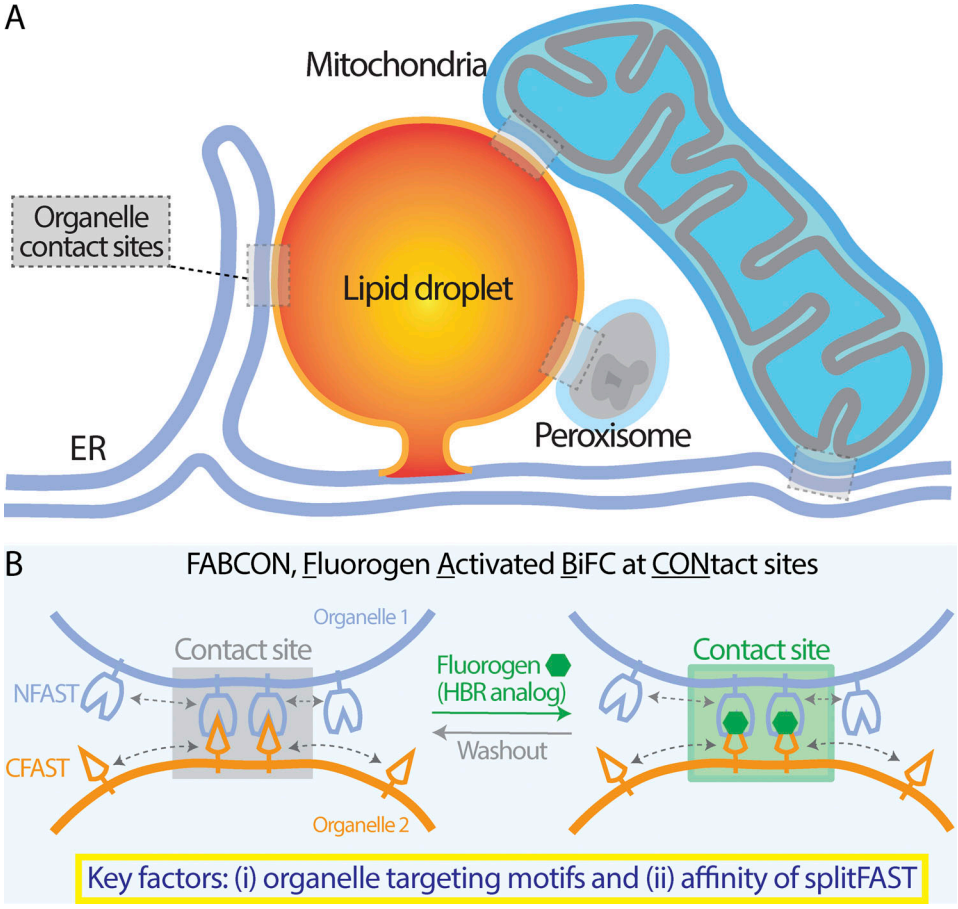

Figure 1. **Visualization of lipid droplet-organelle contact sites using splitFAST-based FABCON. (A)** Organelle contact sites between the endoplasmic reticulum (ER) and lipid droplets (LDs), mitochondria and LDs, peroxisome and LDs, and ER and mitochondria. **(B)** Diagram depicting the implementation of FABCON using a reversible split reporter (splitFAST) and fluorogenic hydroxybenzylidene rhodanine (HBR) analog for detecting organelle contact sites.

further validate the localization of 6xHp, we fused it with APEX2 (Lam et al., 2015), a peroxidase that catalyzes the polymerization and deposition of diaminobenzidine (DAB) in the presence of H_2O_2, creating local electron microscope (EM) contrast. Consistent with the fluorescence microscopy images, we observed strong electron-dense precipitates juxtaposed to lipid droplets via EM in APEX2-6xHp overexpressing U2OS cells following H_2O_2 treatment (Fig. 2 K). Altogether, these results indicate that 6xHp is highly enriched on lipid droplets in multiple cell types, thus making it a suitable targeting motif to bring reporters onto these organelles.

6xHp minimally affects the functions of lipid droplets

Overexpressing synthetic 6xHp may affect native proteins' ability to access lipid droplets via protein crowding (Kory et al., 2015) and compromise the functions of these organelles. We first eliminated these concerns by demonstrating that an endogenous lipid droplet protein, perilipin 2 (PLIN 2), localized on lipid droplets in both control cells and 6xHp-overexpressing cells (Fig. 3 A). In addition, overexpressing 6xHp did not affect the number or size of lipid droplets during biogenesis induced by oleic acid (OA) incubation (Fig. 3, B and C) or breakdown following inhibition of long-chain acyl-CoA synthase by triacsin C treatment (Fig. 3, D and E) (Hartman et al., 1989; Roberts et al., 2023; Tomoda et al., 1987). Using BODIPY staining and low-mag confocal imaging as a readout for total cellular lipid droplet content, we found that 6xHp expressed at low and moderate levels (similar levels for all imaging experiments) minimally perturbed lipid droplet biogenesis (Fig. 3 F) and lipid droplet breakdown (Fig. 3 G). In conclusion, we found that 6xHp is a suitable targeting motif for lipid droplets with negligible perturbation to the functions of these organelles. Targeting motifs for other organelles, including the ER (cytochrome b5 transmembrane domain [Cho et al., 2020] or Sec61β [Greenfield and High, 1999]), mitochondria (SYNJ2BP/OMP25 transmembrane [Benedetti et al., 2020]), and peroxisomes (PMP34), was also validated via a colocalization analysis with known organelle markers (Table S1).

Experimental determination of low-affinity splitFAST for implementing FABCON

The interaction of splitFAST from heterologous organelles constitutes a tether for contact sites. Therefore, the affinity between the cognate pair of splitFAST is crucial to implementing FABCON which only detects but does not create organelle interaction. We first examined whether high-affinity splitFAST (the

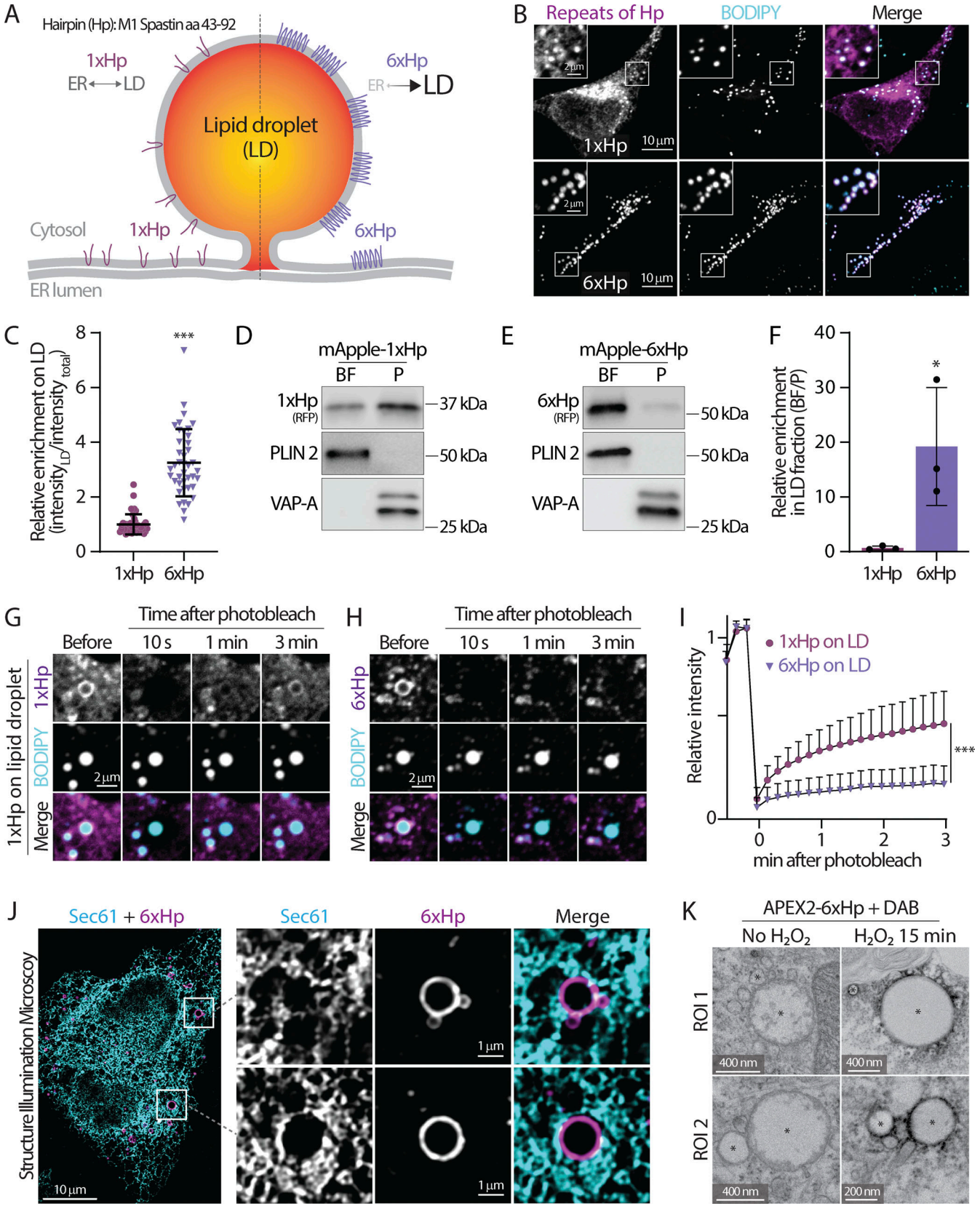

Figure 2. **The design and validation of a synthetic lipid droplet targeting motif. (A)** Diagram depicting the ER and lipid droplet (LD) distribution of 1xHp (hairpin; amino acids 43–92 from human M1 Spastin) and 6xHp. **(B)** Localization of BODIPY 493/503-labeled LDs and mApple-1xHp or mApple-6xHp in HeLa cells treated with 100 µM oleic acid (OA) overnight. Maximal intensity projected (MIP) confocal images from six axial slices (1.8 µm in total thickness) are shown. **(C)** Quantification of relative enrichment of 1xHp and 6xHp on LDs from B. Raw data and mean ± SD are shown (53–56 cells from three independent

experiments). ***P ≤ 0.001, assessed by two-tailed *t* test. **(D and E)** Distribution of mApple-1xHp or mApple-6xHp, LD marker perilipin 2 (PLIN 2), and an ER membrane marker, VAP-A, in sucrose-gradient cellular fractionations from HepG2 cells treated with 200 µM OA. BF, buoyant fraction; P, membrane pellet. **(F)** Quantification of the enrichment of mApple-1xHp or mApple-6xHp in the BF relative to the P fraction in D and E. Data are from three independent experiments (*P ≤ 0.05, assessed by two-tailed *t* test). **(G and H)** Fluorescence recovery after photobleaching (FRAP) of 1xHp (G) and 6xHp (H) on LDs in OA-treated U2OS cells labeled with BODIPY monitored by confocal microscopy. **(I)** Quantification of FRAP of G and H. Mean ± SD are shown (22–37 cells from three or four independent experiments). ***P ≤ 0.001, assessed by two-tailed *t* test. **(J)** Subcellular localization of Halo-6xHp relative to ER marker mEmerald-Sec61β in an OA-treated HeLa cell monitored via structured illumination microscopy. MIP images from 10 axial slices (~2 µm in total thickness) are shown. **(K)** Electron micrographs of LDs in U2OS cells expressing APEX2-6xHp incubated with diaminobenzidine (DAB) in the absence or presence of H_2O_2. * indicates representative LDs. Source data are available for this figure: SourceData F2.

original splitFAST or splitFAST$_{high}$) with a self-complementation K_d of ~3 µM (Rakotoarison et al., 2024; Tebo and Gautier, 2019) affects organelle interaction in the absence of a fluorogen. As compared with control cells expressing mApple-6xHp and ER-targeted HaloTag (Halo-ER), expression of NFAST$_{high}$-mApple-6xHp (NFAST$_{high}$-LD) and CFAST-Halo-ER (CFAST-ER) led to a significant increase of lipid droplet–ER colocalization as a subpopulation of CFAST-ER was enriched with NFAST$_{high}$-LD (Fig. 4, A and C). FRAP analysis further revealed that recovery of CFAST-ER in regions near NFAST$_{high}$-LD was significantly attenuated compared with the bulk of the ER, indicating that CFAST-ER was indeed trapped at ER–LD contact sites via their interaction with NFAST$_{high}$-LD (Fig. 4 B). In contrast, low-affinity splitFAST with a self-complementation K_d of 220 µM

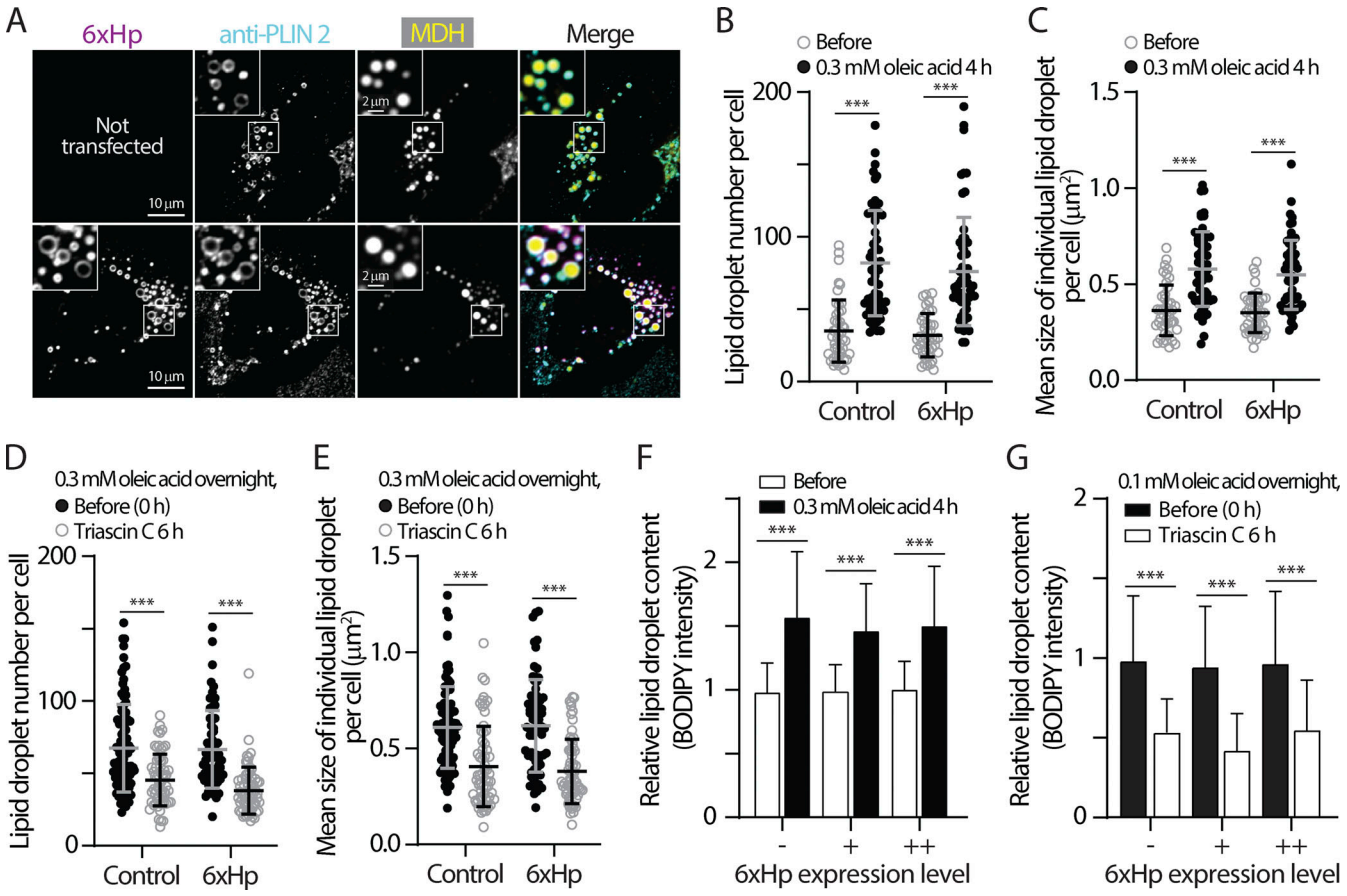

Figure 3. **Minimal perturbation of 6xHp on lipid droplets' properties. (A)** Colocalization of Halo-6xHp and endogenous lipid droplet (LD) protein periplipin 2 (PLIN 2) in an oleic acid (OA)-treated U2OS cell stained with MDH (LD marker) monitored by confocal microscopy. Representative images from a single axial plane (0.3 µm) are shown. **(B and C)** Number and size of LDs in control HeLa cells or in cells overexpressing Halo-6xHp before and after 0.3 mM OA treatment for 4 h. Mean ± SD are shown (43–59 cells from three or four independent experiments). ***P ≤ 0.001, assessed by one-way ANOVA. **(D and E)** Number and size of LDs in OA-loaded HeLa cells with or without Halo-6xHp overexpression before and after 10 µM Triacsin C treatment for 6 h. Mean ± SD are shown (62–96 cells from three or four independent experiments). ***P ≤ 0.001, assessed by one-way ANOVA. **(F)** Relative LD content in HeLa cells overexpressing Halo-6xHp under control conditions or treated with 0.3 mM OA for 4 h. Mean ± SD are shown (98–217 cells from three independent experiments). "–" indicates absence of 6xHp expression. "+" and "++" indicate low and moderate expression of 6xHp, respectively. ***P ≤ 0.001, assessed by one-way ANOVA. **(G)** Relative LD content in OA-loaded HeLa cells overexpressing Halo-6xHp under control conditions or incubated with 10 µM Triacsin C for 6 h. Mean ± SD is shown (169–499 cells from three independent experiments). "–" indicates absence of 6xHp expression. "+" and "++" indicate low and moderate expression of 6xHp, respectively. ***P ≤ 0.001, assessed by one-way ANOVA.

(Rakotoarison et al., 2024) showed similar lipid droplet–ER colocalization to the control level (Fig. 4, A and C). Moreover, CFAST-ER FRAP in regions near $NFAST_{low}$-LD was similar to those in the ER (Fig. 4 B). These results indicated that $NFAST_{high}$-CFAST may lead to the expansion of contact sites while $NFAST_{low}$-CFAST only marginally affects organelle interaction. Consistent with this finding, introducing $NFAST_{high}$ to either the mitochondria ($NFAST_{high}$-mito) or peroxisomes (PX-$NFAST_{high}$) resulted in a significantly higher colocalization with CFAST-LD compared with those in control, with $NFAST_{high}$-mito alone and with $splitFAST_{low}$ pair (Fig. 4, D and E; and Fig. S1, A and B). Importantly, these results demonstrated that, when confined to a membrane (a 2D surface), the reversible bimolecular interaction with sub-μM K_d can drastically interfere with organelle interaction and distribution. Direct measurement of the length of mito-LD contact sites via EM further confirmed that $NFAST_{low}$-CFAST had no effect on the length of contact sites (Fig. 4 F). In conclusion, our data demonstrates that $NFAST_{low}$-CFAST is ideal for implementing FABCON to detect dynamics of contact sites in living cells as it minimally affects organelles' interaction.

We further confirmed that there is no fluorescence leakiness in FABCON. When using HBR-2,5DOM as the fluorogen (Kumar et al., 2024, *Preprint*; Mineev et al., 2021), the signal was only observed when both CFAST-LD and $NFAST_{low}$-ER were present within cells but not in cells with CFAST-LD or $NFAST_{low}$-ER alone (Fig. S1, C and D). The appearance of HBR-2,5DOM signal occurred rapidly following the addition, reached a plateau, and promptly disappeared after the washout (Fig. S1, E and F), reflecting that the splitFAST interaction at contact sites is completely reversible. The addition and washout of 3 μM HBR-2,5DOM also had minimal effects on the length of mito-LD contact sites in cells expressing $NFAST_{low}$-mito and CFAST-LD as detected by EM (Fig. 4, F and G). This indicates that $splitFAST_{low}$ complementation with HBR-2,5DOM reports, but does not create, contact sites under our experimental setup. Altogether, the appearance of the fluorogen signal following HBR-2,5DOM addition most likely reflected splitFAST complementation at pre-existing contact sites. For quantification purposes, we applied only 3 μM of HBR-2,5DOM to circumvent the possibility of enhancing contact site formation associated with a higher concentration of the fluorogen (Kumar et al., 2024, *Preprint*).

In addition, we inserted flexible and helical linkers to the CFAST-containing halves to ensure proper spatial accommodation for splitFAST interaction from heterologous organelles. Based on AlphaFold structure prediction (Jumper et al., 2021), CFAST could explore a space of 5–30 nm from the organelle membrane when the linkers are fully extended (Fig. 4 H). To better control the expression levels of the cognate pairs of splitFAST, we cloned them into a bicistronic IRES backbone and generated lentiviral particles of these IRES plasmids for cellular delivery (Fig. S2, A–D and Table 1). We also kept the HaloTag in the CFAST-containing halves for analysis purposes but replaced the FP in the NFAST-containing halves with spacers and an epitope tag to allow multiplex imaging and validation of expression and localization of all FABCON pairs via confocal microscopy (Fig. S2, A–D).

FABCON reveals the dynamic regulation of ER-LD contact sites

We first examined ER-LD contact sites using FABCON ($FAB^{ER\text{-}LD}$; see Fig. S2 A). In live HeLa cells, ER-LD contact sites appeared to be prevalent and were present on 93% of lipid droplets labeled by CFAST-LD (Table 2), suggesting that most lipid droplets were able to make contact sites with the ER. Among those lipid droplets, 44% had full coverage of ER-LD contact sites while 56% displayed distinguishable domains and were partially covered by these contact sites (Fig. 5 A and Table 2), indicating a heterogenous distribution of ER-LD contact sites within the lipid droplet population. As confocal microscopy has a lateral and axial resolution of ∼250 and ∼500 nm, respectively, we speculate that the full coverage may reflect a collection of signals from unresolved, adjacent ER-LD contact sites of this volume. These properties were consistent in U2OS cells, where 96% of lipid droplets were able to form ER-LD contact sites and 46% of those were partially covered by contact sites (Table 2). These contact site domains may be dynamic as they appear to move along the lipid droplet's surface and change their distribution and intensity within minutes (Fig. 5 B). Lattice light-sheet microscopy (LLSM) provided additional insights into these domains in 3D (Fig. 5 C); whereas lipid droplets' surface is smooth and continuous, ER-LD contact sites displayed uneven distribution and distinct domain structures. Notably, the 3D structure of ER-LD contact sites on each lipid droplet differed from others.

ER-LD contact sites are tethered via many protein complexes, such as the VAP–VPS13 interaction (Kumar et al., 2018; Murphy and Levine, 2016). Therefore, we validated the level of ER-LD contact sites via $FAB^{ER\text{-}LD}$ in VAP-A and VAP-B double knockout (VAP DKO) HeLa cells (Fig. 5 D). In cells expressing similar levels of $FAB^{ER\text{-}LD}$ (Fig. 5 E, left panels), we observed a decrease in ER-LD contact sites in DKO cells (Fig. 5 E, middle and right panels). These cells often displayed clusters of small lipid droplets, and thus, quantifying individual contact sites was technically challenging. To solve this issue, we used the ratio of the $FAB^{ER\text{-}LD}$ signal to that of Halo for expression level normalization as a relative readout for ER-LD contact sites within individual cells. We observed a significant decrease in ER-LD contact sites in VAP DKO cells compared with parental HeLa cells (Fig. 5 F). This indicated that $FAB^{ER\text{-}LD}$ is suitable for detecting native ER-LD contact sites because it reports the expected changes in VAP DKO cells.

Lipid droplets are synthesized at a specialized ER subdomain (Choudhary and Schneiter, 2020; Nettebrock and Bohnert, 2020) and can be induced with the exogenous addition of fatty acids (Nakajima et al., 2019). An increase in ER-LD interactions is expected during lipid droplet biogenesis; however, the dynamics of their interactions is not well understood. Following an incubation period at a high concentration of OA (500 μM), we observed a significant (∼45%) increase in ER-LD contact sites at 1 h (Fig. 5 G), illustrating the correlation of these sites to lipid droplet formation (de Vries et al., 1997; Fujimoto et al., 2007). Intriguingly, this increase was transient as ER-LD contact sites decreased and returned to the baseline level after 2 h (Fig. 5 G). These dynamic changes in ER-LD contact sites during biogenesis were not correlated to changes in the number and size of lipid droplets (Fig. S3, A and B), suggesting that the FABCON readout

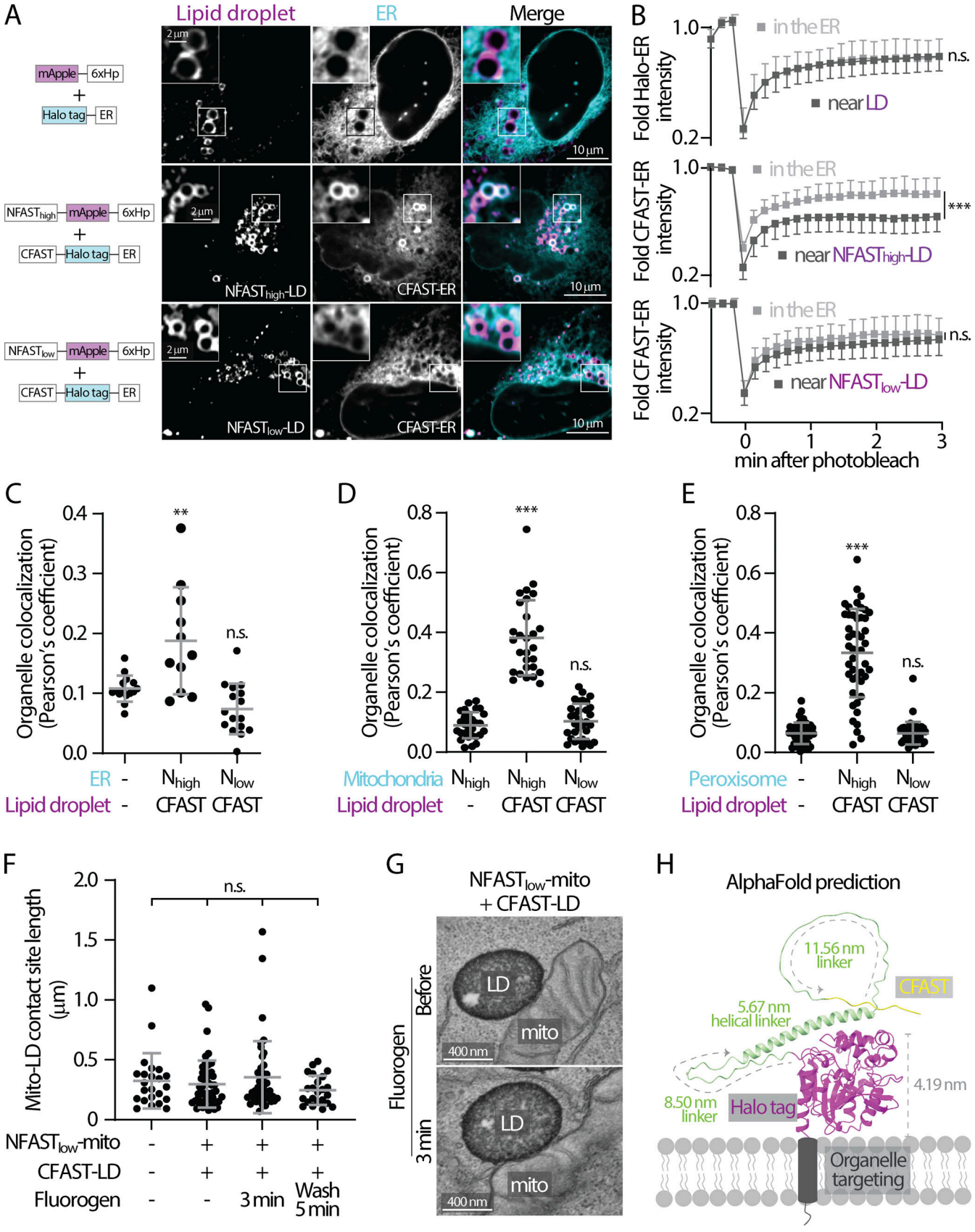

Figure 4. **Low affinity splitFAST is suitable for implementing FABCON. (A)** Distribution of mApple-6xHp and Halo-ER (top), NFAST$_{high}$-mApple-6xHp and CFAST-Halo-ER (middle), and NFAST$_{low}$-mApple-6xHp and CFAST-Halo-ER (bottom) in an oleic acid (OA)-treated U2OS cell. Representative images from a single axial plane are shown. **(B)** Quantification of fluorescence recovery after photobleaching of Halo-ER in the endoplasmic reticulum (ER) and near lipid

droplets (LDs); or CFAST-Halo-ER in the ER and near $NFAST_{high}$- or $NFAST_{low}$-decorated LDs. Mean ± SD is shown (20–25 regions from three independent experiments). n.s. = not significant, ***P ≤ 0.001, unpaired *t* test, two-tailed. **(C)** Quantification of the Pearson's colocalization coefficient of LDs and ER described in A. Raw data and mean ± SD are shown (11–16 cells from three independent experiments). **P ≤ 0.01, assessed by one-way ANOVA. **(D)** Quantification of the Pearson's colocalization coefficient of LDs and mitochondria (mito) in cells expressing Halo-6xHp and $NFAST_{high}$-mApple-mito, CFAST-Halo-6xHp and $NFAST_{high}$-mApple-mito, or CFAST-Halo-6xHp and $NFAST_{low}$-mApple-mito (see Fig. S1 A). Raw data and mean ± SD are shown (29–32 cells from three independent experiments). ***P ≤ 0.001, assessed by one-way ANOVA. **(E)** Quantification of the Pearson's colocalization coefficient of LDs and peroxisomes described in cells producing Halo-6xHp and PMP34-mApple, CFAST-Halo-6xHp and PMP34-mApple-$NFAST_{high}$, or CFAST-Halo-6xHp and PMP34-mApple-$NFAST_{low}$ (see Fig. S1 B). Raw data and mean ± SD are shown (44–51 cells from three independent experiments). ***P ≤ 0.001, assessed by one-way ANOVA. **(F)** Quantification of the length of mito-LD contact sites detected by scanning transmission electron microscopy (STEM) in control HeLa cells or cells expressing $FAB^{mito\text{-}LD}$ in the absence, 3 min after the addition, and 5 min after the washout of 3 µM HBR-2,5DOM. Raw data and mean ± SD are shown (*n* = 23 in control; *n* = 50 in N_{low}+CFAST without dye; *n* = 43 in N_{low}+CFAST with dye; *n* = 23 in N_{low}+CFAST after washout). *n*.s. = not significant, assessed by one-way ANOVA. **(G)** Representative electron micrographs of mito-LD contact sites detected by STEM in HeLa cells expressing $FAB^{mito\text{-}LD}$ in the absence and presence of 3 µM HBR-2,5DOM for 3 min. **(H)** AlphaFold structure prediction of CFAST-linker-Halo displayed on a membrane bilayer. The size of Halo tag and length of flexible and helical linkers are indicated.

reflects the extent of contact sites rather than the abundance of organelles present.

Seipin is an ER membrane protein that regulates lipid droplet size during biogenesis by bridging the membrane continuum between the ER and lipid droplets (Fei et al., 2008, 2011; Salo et al., 2016, 2019; Wang et al., 2016). Knowing this, we wondered if seipin plays a role in the formation of ER-LD contact sites. Consistent with previous studies (Salo et al., 2016; Wang et al., 2016), we found that lipid droplets in seipin knockout (KO) cells were heterogenous in size, with a few larger ones compared to wild-type cells (Fig. 5, H and I, left panels). Intriguingly, we observed a significant increase in ER-LD contact sites in seipin KO cells either under low (20 µM) or high (100 µM) OA incubation, conditions that mimic a resting state or fatty acid surplus, respectively (Fig. 5, I and J). Altogether, we found that FABCON was able to detect ER-LD contact sites with high spatial precision and revealed dynamic changes in these sites following a variety of stimuli and manipulations.

Dynamic regulation of mito-LD contact sites during metabolic switching

We next characterized mito-LD contact sites using $FAB^{mito\text{-}LD}$ (Fig. 6 A and Fig. S2 B). Similar to what we observed in ER-LD contact sites, ∼90% of lipid droplets were competent to make contact sites with mitochondria in HeLa and U2OS cells (Table 2). Interestingly, among the lipid droplets that can form contact sites, only 20% were fully covered with mito-LD contact sites while the other 80% often displayed distinct contact site domains (partial coverage). These observations suggested that mito-LD contact sites were less prevalent on the lipid droplet surface compared to ER-LD contact sites. Moreover, mito-LD contact sites often outlined the perimeter of lipid droplet clusters but were less common in the central region of these clusters (Fig. 6 A, bottom panels). In addition, some mito-LD contact site domains were dynamic as they appeared to fuse and move along the lipid droplet's surface within minutes (Fig. 6 B).

Recent studies demonstrated that perilipin 5 (PLIN 5) is a tether for mito-LD contact sites (Miner et al., 2023; Ouyang et al., 2023; Wang et al., 2011). Therefore, we examined the levels of mito-LD contact sites in PLIN 5 knockdown HeLa cells (Fig. 6, C and D). We found a moderate yet significant reduction in mito-LD contact sites in siPLIN 5-treated HeLa cells following 100 µM OA incubation (Fig. 6 E), suggesting that PLIN 5 tethers lipid droplets to mitochondria under fatty acid surplus conditions. In contrast, wild-type and VAP DKO HeLa cells showed similar levels of mito-LD contact sites (Fig. 6 E) as VAP-A and VAP-B are ER-resident proteins that have no direct role in mito-LD tethering. In addition, knocking out a PX-LD tether, M1 Spastin, had no effect on the formation of mito-LD contact sites (Fig. 8, B and D). These data suggest that mito-LD contact sites are independently maintained regardless of the status of other lipid droplet–organelle interactions.

Mitochondria are essential for fatty acid oxidation (FAO) to generate ATP. We reasoned that mito-LD contact sites may be regulated when switching to FAO-dependent conditions as these sites can facilitate fatty acid trafficking. To test this idea, we monitored mito-LD contact sites following OA withdrawal in HeLa cells treated with 100 µM OA overnight. We observed a transient increase in mito-LD contact sites 1 h after incubating these OA-loaded cells in control media (Fig. 6 F, left). In contrast, a sustained increase in mito-LD contact sites was observed in cells treated with 10 µM isoproterenol (Fig. 6 F, middle), a drug known to induce lipolysis (Gallardo-Montejano et al., 2016).

Table 1. **SplitFAST pairs for contact sites**

Contact sites	NFAST half	CFAST half	IRES plasmid (5′-3′)
ER-LD	$NFAST_{low}$-ER	CFAST-LD	$NFAST_{low}$-ER_IRES_CFAST-L-LD
Mito-LD	$NFAST_{low}$-mito	CFAST-LD	$NFAST_{low}$-mito_IRES_CFAST-L-LD
PX-LD	PX-$NFAST_{low}$	CFAST-LD	PX-$NFAST_{low}$_IRES_CFAST-L-LD
ER-mito	$NFAST_{low}$-ER	CFAST10-mito	$NFAST_{low}$-ER_IRES_CFAST10-L-mito

ER, endoplasmic reticulum; LD, lipid droplet; mito, mitochondria; PX, peroxisome; L, linker.

Table 2. **Contact sites statistics**

Cell type	Contact sites	% LD with contact sites	Full coverage (% LD with contact site)	Partial coverage	Standard deviation
HeLa	ER-LD	93%	43.95%	56.05%	3.82
U2OS	ER-LD	96%	54.25%	45.75%	5.38
HeLa	Mito-LD	86%	17.33%	82.67%	2.98
U2OS	Mito-LD	94%	23.67%	76.33%	4.84
U2OS	PX-LD	66%	7.24%	92.76%	5.50

ER, endoplasmic reticulum; LD, lipid droplet; mito, mitochondria; PX, peroxisome.

These results indicated that the level of mito-LD contact sites was correlated with fatty acid release from lipid droplets. Interestingly, treatment with 2DG, which inhibits glycolysis and likely enhances FAO (Brown, 1962; Shiratori et al., 2019; Sottnik et al., 2011), during OA withdrawal ultimately resulted in a peaked increase in mito-LD contact sites at 2 h before levels dropped below the baseline level after 8 h (Fig. 6 F). Consistent with ER-LD readouts, changes in mito-LD contact sites were not correlated with the number nor size of lipid droplets (Fig. S3, C and D). Altogether, these data revealed differential regulation of mito-LD contact sites under various metabolic conditions.

Automated contact site analysis

The domains of ER-LD and mito-LD contact sites could be easily observed on larger lipid droplets in U2OS cells. To further quantify these domains, we developed an automated line-scanning analysis pipeline for unbiased contact site mapping (COSIMA). The COSIMA pipeline involves the following: (i) a machine learning–based identification of the outline and void of lipid droplets using ilastik, (ii) a Python-based traverse algorithm to measure the intensity of FABCON (contact site) and Halo (lipid droplet) channels along the edges of the voids, and (iii) the generation of intensity profiles (Fig. 7 A). We included a collision detection process within the traverse algorithm to eliminate duplicated data from two connected lipid droplets (see Materials and methods). We manually picked lipid droplets with distinguishable contact site domains and defined the size of the domains by measuring the distance between local intensity minima (Fig. 7 A, bottom right). The average size of lipid droplets we analyzed for ER-LD and mito-LD contact sites was similar (Fig. 7 B), ruling out lipid droplets' size as a contributing factor to the following results. The minimal size of contact sites from this analysis was 0.237 µm (Fig. 7 C, in the mito-LD group), which is consistent with the lateral resolution of confocal microscopy.

After analyzing more than 80 domains from each group, we found that the domain size of ER-LD ranged from 0.29 to 7.87 µm with a mean of 2.39 µm (Fig. 7 C). A similar range of domain size was found in the mito-LD group: 0.24–7.86 µm with a mean of 2.41 µm. Interestingly, all normality tests rejected normal population distribution of contact site length from the two groups (Table 3). Histograms of domain size from both contact sites were indicative of multimodal distribution (Fig. 7, D and E). Based on the estimated parameters derived from the Gaussian mixture model analysis, it is evident that the ER-LD data exhibits a 47.1% probability of originating from a normal distribution with a mean of 1.29 and an SD of 0.61: N1 (1.29, 0.61), and a 52.9% probability of originating from another normal distribution N2 (3.37, 1.45) (Fig. 7 D, traces). Similarly, the mito-LD data demonstrates a 53.2% probability of originating from a normal distribution N1 (1.32, 0.52), and a 46.8% probability of originating from a larger normal distribution N2 (3.65, 1.57) (Fig. 7 E, traces). Notably, the ER-LD data exhibits a higher likelihood of being generated from the larger Gaussian distribution. These results demonstrated that the sizes of individual contact sites were heterogeneous and suggested distinct spatial determinants for each contact site subpopulation.

In addition, each lipid droplet harbored an average of 2.07 ER-LD contact sites which covered 61.7% of the lipid droplet's circumference (Fig. 7, F and G). In contrast, mito-LD contact sites only occupied 48.75% of the perimeter of a lipid droplet (Fig. 7 G), which was primarily due to only 1.70 mito-LD contact sites per lipid droplet (Fig. 7 F). Interestingly, contact sites of various sizes can exist on the same lipid droplets (Figs. 5 B, 6 B, 7 A, and 8 A). Overall, these analyses are consistent with the observation that ER-LD contact sites are more prevalent on lipid droplets than mito-LD contact sites (Table 2).

FABCON is generalizable to visualize organelle contact sites

To demonstrate the generalizability of FABCON, we focused on PX-LD and ER-mito contact sites. As detected by $FAB^{PX\text{-}LD}$ (Fig. S2 C and Fig. 8 A), PX-LD was the least abundant contact site of lipid droplets. In U2OS cells, only 66% of lipid droplets could make contact sites with peroxisomes; among these lipid droplets, 93% displayed partial coverage on lipid droplets (Fig. 8 A and Table 2). When $FAB^{PX\text{-}LD}$ was expressed in Spastin KO cells, a moderate reduction was detected for PX-LD contact sites (Fig. 8, B and C), consistent with the role of M1 Spastin as a tether protein for PX-LD contact sites (Chang et al., 2019). Our data also suggested additional PX-LD tethering mechanisms exist. In contrast to the low occurrence of PX-LD contact sites, ER-mito contact sites revealed by $FAB^{ER\text{-}mito}$ (implemented with CFAST10 of lower affinity, see Fig. S2 D) (Tebo and Gautier, 2019) were abundant and distributed throughout the entire cell (Fig. 8 E). ER-mito contact sites appeared to be distinct foci of various size and intensity along mitochondria (Fig. 8 E, inset; Fig. 8 F). In summary, our data demonstrated that FABCON is

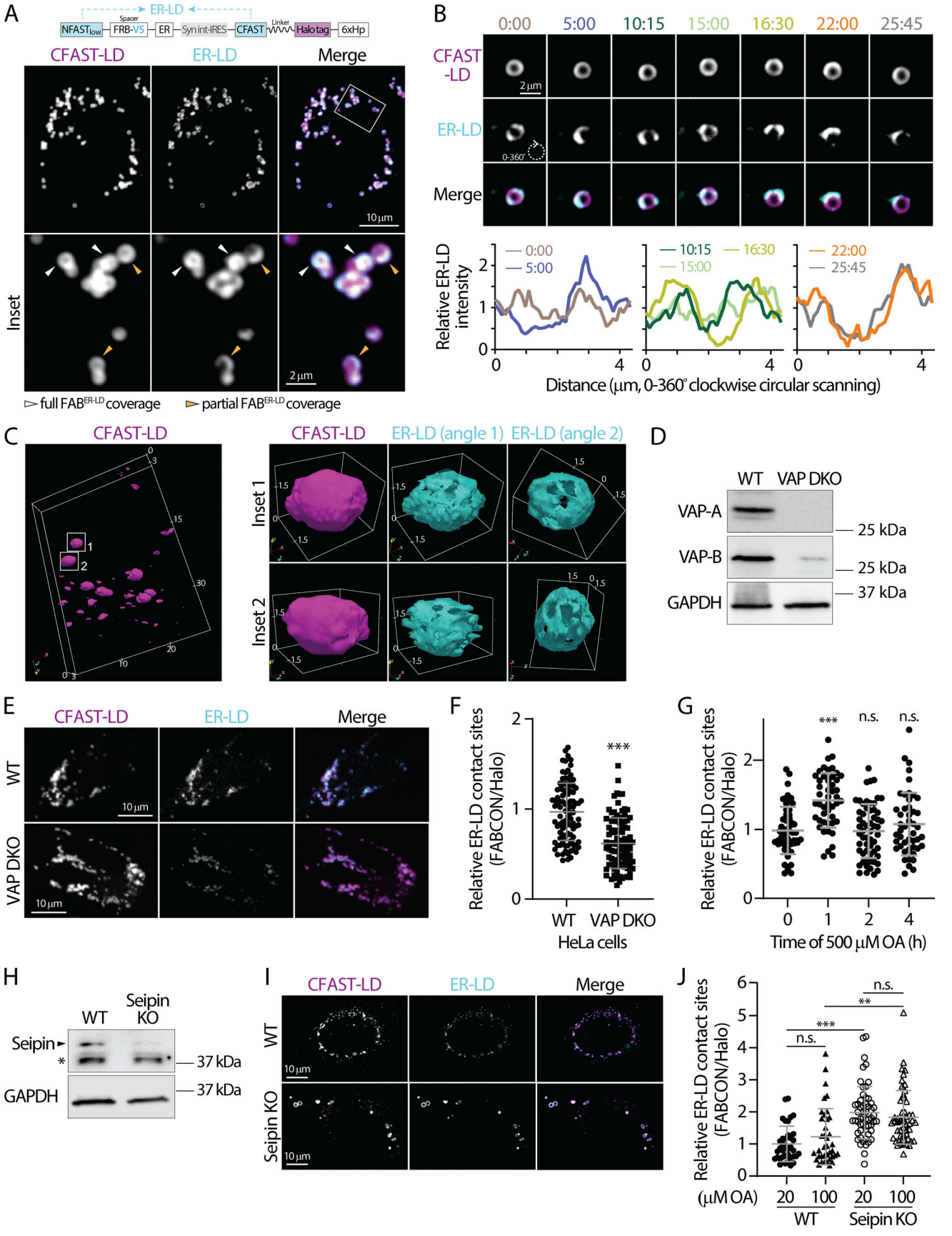

Figure 5. **Dynamic regulation of ER-LD contact sites revealed via FAB^{ER-LD}. (A)** Detection of lipid droplets (LDs) and endoplasmic reticulum (ER)-LD contact sites in oleic acid (OA)-treated HeLa cells producing FAB^{ER-LD} (top) monitored by confocal microscopy. Representative maximal intensity projected

images from three axial slices (~1 µm in total thickness) are shown in bottom panels. **(B)** Dynamics of ER-LD contact sites on an LD in OA-treated U2OS cell producing $FAB^{ER\text{-}LD}$ monitored by confocal microscopy over time (top). Relative intensity profiles of ER-LD contact sites measured by clockwise circular scanning are shown in bottom panels. **(C)** 3D rendering of LDs and ER-LD contact site in U2OS cells imaged via LLSM. LDs labeled by CFAST-LD from a whole cell are shown on the left. Box volume is 24.6 × 16.8 × 2.67 µm. Two individual LDs and their ER-LD contact sites are shown on the right. Box volumes are 3.10 × 2.35 × 2.52 µm (top row) and 3.28 × 2.40 × 2.82 µm (bottom row). Numbers indicate distance (µm). **(D)** Protein levels of VAP-A and VAP-B in wild-type (WT) and VAP double knockout (DKO) HeLa cells detected by Western blot. **(E)** ER-LD contact sites in WT and VAP DKO HeLa cells producing $FAB^{ER\text{-}LD}$ monitored by confocal microscope. Representative maximal intensity projected images from three axial slices (~1 µm in total thickness) are shown. **(F)** Quantification of the relative levels of ER-LD contact sites in control and VAP DKO HeLa cells. Raw data and mean ± SD are shown (96 cells for each condition from three independent experiments) ***P ≤ 0.001, assessed by two-tailed *t* test. **(G)** Relative levels of ER-LD contact sites HeLa cells pulsed with 500 µM of OA over time. Raw data and mean ± SD are shown (47–58 cells from three independent experiments). n.s. = not significant, ***P ≤ 0.001, assessed by one-way ANOVA and Dunnett's multiple comparisons test with 0 h as the control group. **(H)** Protein level of Seipin in WT and Seipin KO SUM159 cells detected by Western blot. * indicates non-specific band of detection. **(I)** ER-LD contact sites in oleic acid (OA)-treated WT and Seipin KO SUM159 cells producing $FAB^{ER\text{-}LD}$ monitored using confocal microscopy. Representative maximal intensity projected images from three axial slices (~1 µm in total thickness) are shown. **(J)** Relative levels of ER-LD contact sites in WT and Seipin KO SUM159 cells producing $FAB^{ER\text{-}LD}$ and treated with 20 or 100 µM OA overnight. Raw data and mean ± SD are shown (37–55 cells from four independent experiments). n.s. = not significant, ***P ≤ 0.001, assessed by one-way ANOVA. Source data are available for this figure: SourceData F5.

readily applicable to detect any contact sites of interest providing proper organelle-targeting motifs.

Discussion

Organelle contact sites are important subcellular architecture of functional integration by providing a platform for interorganelle transport of a variety of biomolecules, positioning organelles, and facilitating organelle morphogenesis (Abrisch et al., 2020; Lee et al., 2020; Prinz et al., 2020). Since the initial observations of contact sites via EM in 1950s (Palade, 1952; Porter and Palade, 1957), significant progress has been made in uncovering mechanistic and functional insights into these minute foci. Nonetheless, determining how these nanoscale subcellular foci are dynamically regulated remains challenging due to the limited spatial-temporal resolution of imaging technologies. During the past decade, proximity-induced reporters, such as split FP (Cieri et al., 2018; Eisenberg-Bord et al., 2016; Harmon et al., 2017; Kakimoto et al., 2018; Shai et al., 2018), dimerized-dependent FP (ddFP) (Alford et al., 2012; Miner et al., 2024), and fluorescence resonance energy transfer FP pairs (Csordás et al., 2010; Naon et al., 2016; Poteser et al., 2016; Venditti et al., 2019; Wong et al., 2018), have been applied to probe organelle proximity at contact sites. Though these approaches are generalizable and straightforward to apply, the implementation has encountered many roadblocks, including irreversibility, fluorescence leakiness, and low signal-to-noise readout. We aimed to use splitFAST to implement this proximity-induced reporter approach to circumvent these difficulties. After vigorous engineering and validation using synthetic biology, LM, EM, and basic biochemistry, we successfully implemented FABCON to dynamically detect ER-LD, mito-LD, PX-LD, and ER-mito contact sites. FABCON's overall advantages include reversibility, low fluorescence background, and straightforward quantification based on FABCON intensity.

We had to first overcome the challenging issue of lipid droplet targeting by engineering synthetic 6xHp based on M1 Spastin's Hp motif (Chang et al., 2019). 6xHp displayed significant enrichment on lipid droplets and minimal ER distribution upon expression at moderate levels, which greatly facilitated the implementation of FABCON. We envision that 6xHp will allow us to bring other reporters onto the surface of lipid droplets for additional applications such as proximity labeling-proteomics. Though 6xHp minimally affected lipid droplets' functions when transiently introduced into cells, the predicted molecular weight of 6xHp is over 35 kDa and it is expected to be highly hydrophobic as mApple-6xHp migrated faster than expected in SDS-PAGE. Further optimization is needed to overcome these limitations.

Another unexpected engineering issue is related to the affinity of splitFAST. To our surprise, $splitFAST_{high}$ of sub-µM K_d significantly altered organelle distribution and interaction while $splitFAST_{low}$ of 220 µM K_d has minimal effects on organelle contact sites. Confining splitFAST to 2D membranes could substantially enhance their effective K_d at organelle contact sites. Nonetheless, compared with rapamycin-induced FRB-FKBP dimerization with a K_d at sub-nM range (Banaszynski et al., 2005), the affinity of $splitFAST_{high}$ self-complementation was rather weak, yet still strong enough to drive contact sites formation. This suggests that the bimolecular complementation of a sub-µM K_d reporter at organelle contact sites is practically irreversible. We speculated that the irreversible traditional split FPs at contact sites would significantly remodel organelle distribution, leading to cellular stress and/or adaptation. Another affinity-related issue is the stabilization of NFAST-CFAST complementation upon the addition of a fluorogen, which can potentially expand contact sites (Kumar et al., 2024, *Preprint*; Rakotoarison et al., 2024; Tebo and Gautier, 2019). To minimize the stabilization issue, we used a low concentration (<3 µM) of the fluorogen and only performed imaging experiments shortly after the addition. Quantification of experiments with higher fluorogen concentrations or with incubation periods over 30 min needs to be further validated. Overall, our observations suggest that organelle contact sites are likely maintained and subjected to rapid turnover via a collection of weak endogenous tethers. The affinity of organelle interaction at contact sites remains an open question. Further work using the splitFAST pairs and/or fluorogens with a wide range of complementation affinities (Kumar et al., 2024, *Preprint*; Rakotoarison et al., 2024) will better visualize native contact sites and help provide needed quantitative information about the affinity of organelle tethering at contact sites.

Built on the current understanding that ER-LD contact sites are important for lipid droplet biogenesis (Hugenroth and

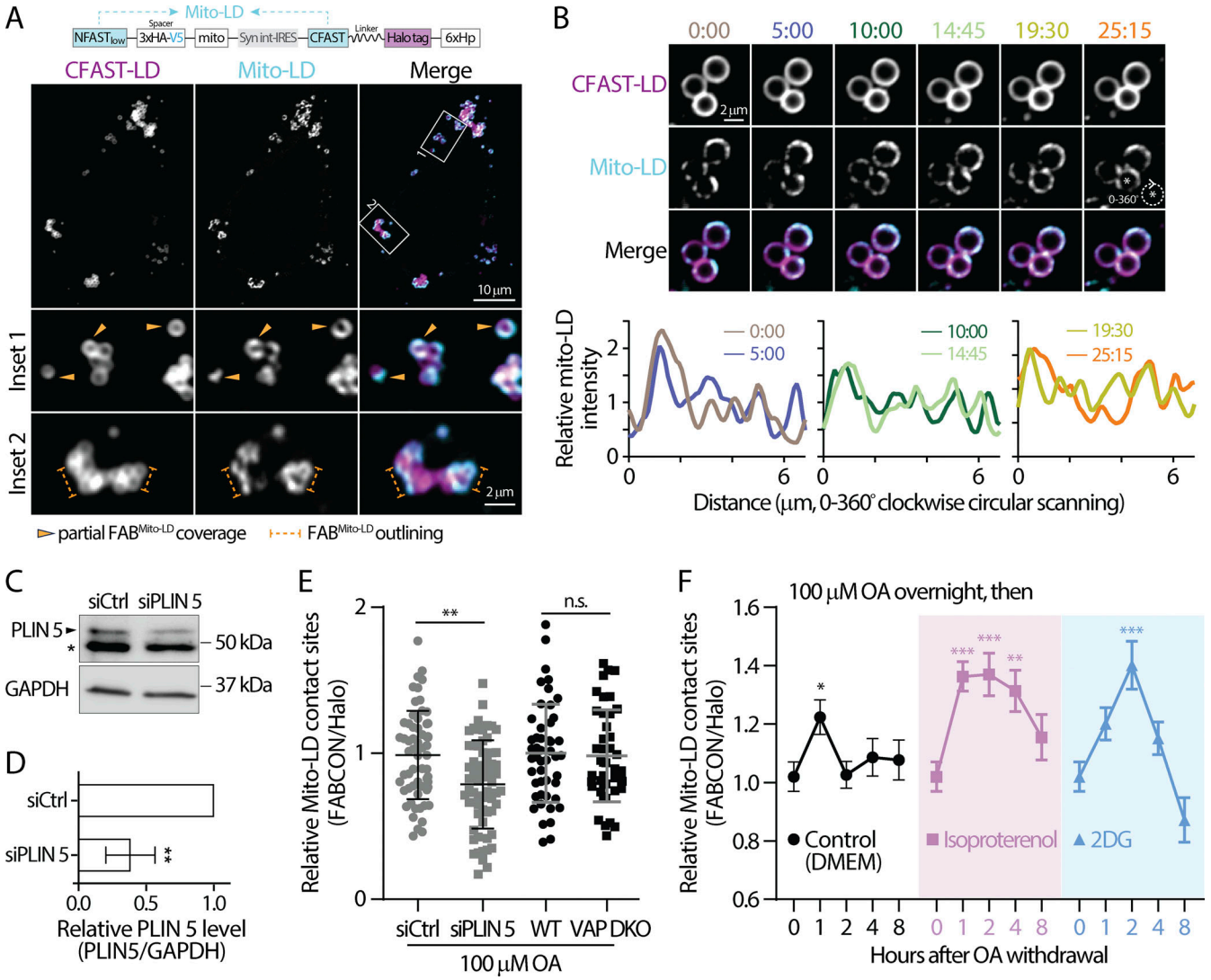

Figure 6. **Dynamic regulation of mito-LD contact sites revealed via FAB$^{mito\text{-}LD}$. (A)** Detection of lipid droplets (LDs) and mitochondria (mito)-LD contact sites in oleic acid (OA)-treated HeLa cells producing FAB$^{mito\text{-}LD}$ (top) monitored via confocal microscopy. Representative maximal intensity projected images from two axial slices (0.6 µm in total thickness) are shown in bottom panels. **(B)** Dynamics of mito-LD contact sites on a LD in OA-treated U2OS cell producing FAB$^{mito\text{-}LD}$ monitored by confocal microscopy over time (top). Relative intensity profiles of mito-LD measured by clockwise circular scanning are shown in the bottom panels. **(C)** Perilipin 5 (PLIN 5) levels in HeLa cells transfected with scramble (siCtrl) or PLIN 5 siRNA detected by Western blot. * indicates non-specific band. **(D)** Quantification of relative PLIN 5 level described in C. Data are from three independent experiments (**P ≤ 0.01, unpaired *t* test, two-tailed). **(E)** Relative levels of mito-LD contact sites in OA-treated HeLa cells transfected with scramble or PLIN 5 siRNA. Raw data and mean ± SD are shown (61–63 cells from three independent experiments). n.s. = not significant, **P ≤ 0.01, assessed by two-tailed *t* test. **(F)** The temporal dynamics of mito-LD contact sites in OA-treated HeLa cells following OA withdrawal in DMEM and in DMEM with 10 µM of isoproterenol or 4 mM 2DG. Mean ± SE are shown (37–58 cells from three or four independent experiments). Statistical significance was compared to time zero by one-way ANOVA. **P ≤ 0.01; ***P ≤ 0.001. Source data are available for this figure: SourceData F6.

Bohnert, 2020), FAB$^{ER\text{-}LD}$ further revealed the temporal correlation of these sites during this process. We speculate that ER-LD contact sites provide a spatial platform for lipid and/or fatty acid trafficking to fuel the initial growth of lipid droplets, and their association with the ER may need to be relaxed for further lipid droplet expansion. The negative correlation between seipin and ER-LD contact sites is another interesting observation. Seipin bridges the membrane continuum between ER and lipid droplets and appears to be important for the even distribution of fatty acids into individual lipid droplets as seipin KO cells possessed lipid droplets of various sizes but showed minimal defects in total neutral lipid content (Salo et al., 2019; Wang et al., 2016). EM further revealed that lipid droplets made a wide range of contact sites, from no interaction to extensive coverage, with the ER in seipin KO cells (Salo et al., 2016; Wang et al., 2016); however, the prevalence of distinct types of contact sites remains unclear. Our results showed that overall seipin KO cells have a higher level of ER-LD contact sites. In addition, FABCON could provide a contact site readout for individual, spatially separate lipid droplets, which will help answer questions related to how contact sites are distributed and correlated throughout the lipid droplet population.

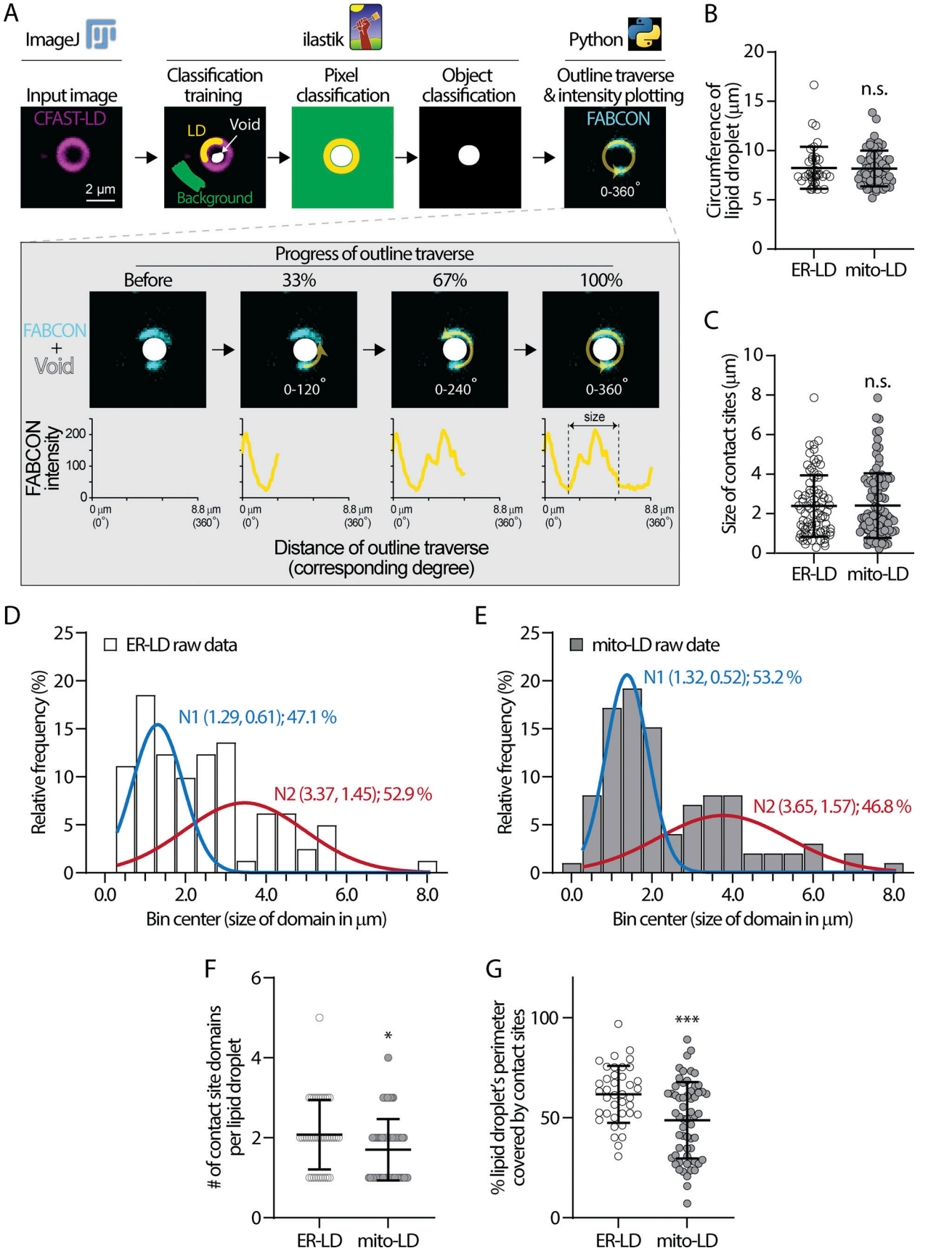

Figure 7. **COSIMA analysis of ER-LD and mito-LD contact sites. (A)** A flowchart describing the COSIMA pipeline. **(B)** Circumference of lipid droplets (LDs) analyzed by COSIMA in the endoplasmic reticulum (ER)-LD and mitochondria (mito)-LD group. Raw data and mean ± SD are shown (39–60 LDs). n.s. = not

significant, assessed by two-tailed *t* test. **(C)** Size of ER-LD and mito-LD contact sites measured by COSIMA. Raw data and mean ± SD are shown (81–99 contact sites). n.s. = not significant, assessed by two-tailed *t* test. **(D and E)** Population distribution of domain size of ER-LD (D) and mito-LD (E) contact sites. Bar graphs show raw data and traces represent fitted bi-modal Gaussian distributions (N). Each N is shown as (mean, SD); % of raw data. **(F)** Number of ER-LD and mito-LD contact sites on each LD. Raw data and mean ± SD are shown (39–60 LDs). *P ≤ 0.05, assessed by two-tailed *t* test. **(G)** Fraction of LD's perimeter covered by ER-LD and mito-LD contact sites. Raw data and mean ± SD are shown (39–60 LDs). ***P ≤ 0.001, assessed by two-tailed *t* test.

The association between mitochondria and lipid droplets is expected to play an important role in mitochondrial FAO and cellular energetics. While many reports have shown a correlation between mito-LD contact sites and fatty acid trafficking and oxidation (Rambold et al., 2015; Sadh et al., 2017; Talari et al., 2023; Wang et al., 2021), others have demonstrated that lipid droplet–associated mitochondria have low FAO activity (Najt et al., 2023). Our data from FAB$^{mito\text{-}LD}$ may help explain this discrepancy from a temporal point of view. Although mito-LD contact sites are generally upregulated following isoproterenol and 2DG treatment, the extent of upregulation during these conditions is markedly distinct. This temporal information will help guide future mechanistic studies. Further investigation into how mito-LD contact sites are regulated in physiologically relevant cell types, such as hepatocytes, muscle cells, or adipocytes, may shed light on the contribution of these sites to cellular energetics.

The reversibility of FABCON provides a wider temporal window to monitor the dynamics of organelle contact sites upon stimulation. We demonstrated that both ER-LD and mito-LD contact sites are dynamically regulated upon distinct manipulation at the cellular level. We envision that FABCON can be used as a reliable readout to address the mechanisms behind these regulations. In addition, FABCON revealed the heterogeneity of contact sites at a single-lipid droplet level, which will help answer questions related to an organelle's ability to form contact sites and to the subcellular distribution of individual contact sites. Furthermore, our data demonstrated that FABCON can provide an intensity-based readout for the levels of contact sites, indicating the possibility of large-scale screening using flow cytometry.

Table 3. **Test for normal distribution**

Test	mito-LD	ER-LD
D'Agostino & Pearson test		
P value	<0.0001	0.0015
Passed normality test (alpha = 0.05)?	No	No
Anderson–Darling test		
P value	<0.0001	0.0002
Passed normality test (alpha = 0.05)?	No	No
Shapiro–Wilk test		
P value	<0.0001	0.0001
Passed normality test (alpha = 0.05)?	No	No
Kolmogorov–Smirnov test		
P value	<0.0001	0.0204
Passed normality test (alpha = 0.05)?	No	No

To systematically analyze FABCON-derived data of higher spatial precision and acquire statistically meaningful information, we created an automated line scanning pipeline, COSIMA, based on open-source software and codes. COSIMA revealed that the sizes of contact site domains are heterogeneous; contact sites of different lengths could be found on the same lipid droplets. This observation raised possibilities such as the following: (i) contact sites of different sizes are maintained via a distinct set of tethers and likely create functional segregation and/or (ii) the size reflects the available lipid droplet surface for contact sites due to physical confinements. Our approach combined with other manipulations may provide insights into lipid droplet-organelle contact site heterogeneity. With reasonable modifications and optimizations, this pipeline can be readily applied for line scanning on the perimeter of any enclosed objects, such as individual mitochondria or phase condensates.

We envision the next phase for the development of FABCON is the generation of orthogonal splitFAST reporters to detect multiple contact sites simultaneously. We did not explore green- and red-splitFAST because they appear to have a comparable affinity as splitFAST$_{high}$ (Tebo et al., 2021). We have tried split UnaG, another reversible fluorogenic split reporter (To et al., 2016), but did not observe a signal at contact sites (data not shown). One possibility is to utilize split Halo tag and recently developed reversible Halo ligands (Huppertz et al., 2024; Ishikawa et al., 2012; Kompa et al., 2023; Minner-Meinen et al., 2021; Shao et al., 2021) to develop orthogonal split FPs that work with splitFAST. Additionally, it may be possible to combine FABCON with other ddFP-based tool kits to investigate multiple contact sites (Alford et al., 2012; Miner et al., 2024). Overall, our work provides a new tool kit for the detection of lipid droplet–organelle contact sites and beyond. Through our findings, we have demonstrated that FABCON is capable of revealing the dynamics of contact sites and generating observation-based hypotheses to further understand the complex interaction between organelles.

Materials and methods

Cell lines, transient transfection, and general reagents

HeLa, U2OS, and HepG2 cells were purchased from American Type Culture Collection (ATCC) and were maintained in media following ATCC's recommendations. VAP DKO and parental HeLa cells (HeLa-HFT) were provided by Dr. Wade Harper at Harvard Medical School (Boston, MA, USA) and grown in Eagle's minimal essential medium (EMEM, Thermo Fisher Scientific) with 10% fetal bovine serum (FBS) and 1X penicillin/streptomycin solution (Corning). In brief, VAP-DKO cells were gene-edited from HeLa-HFT cells (Heo et al., 2015) to ablate VAP-A and VAP-B. Seipin KO and wild-type SUM159 cells (Wang et al.,

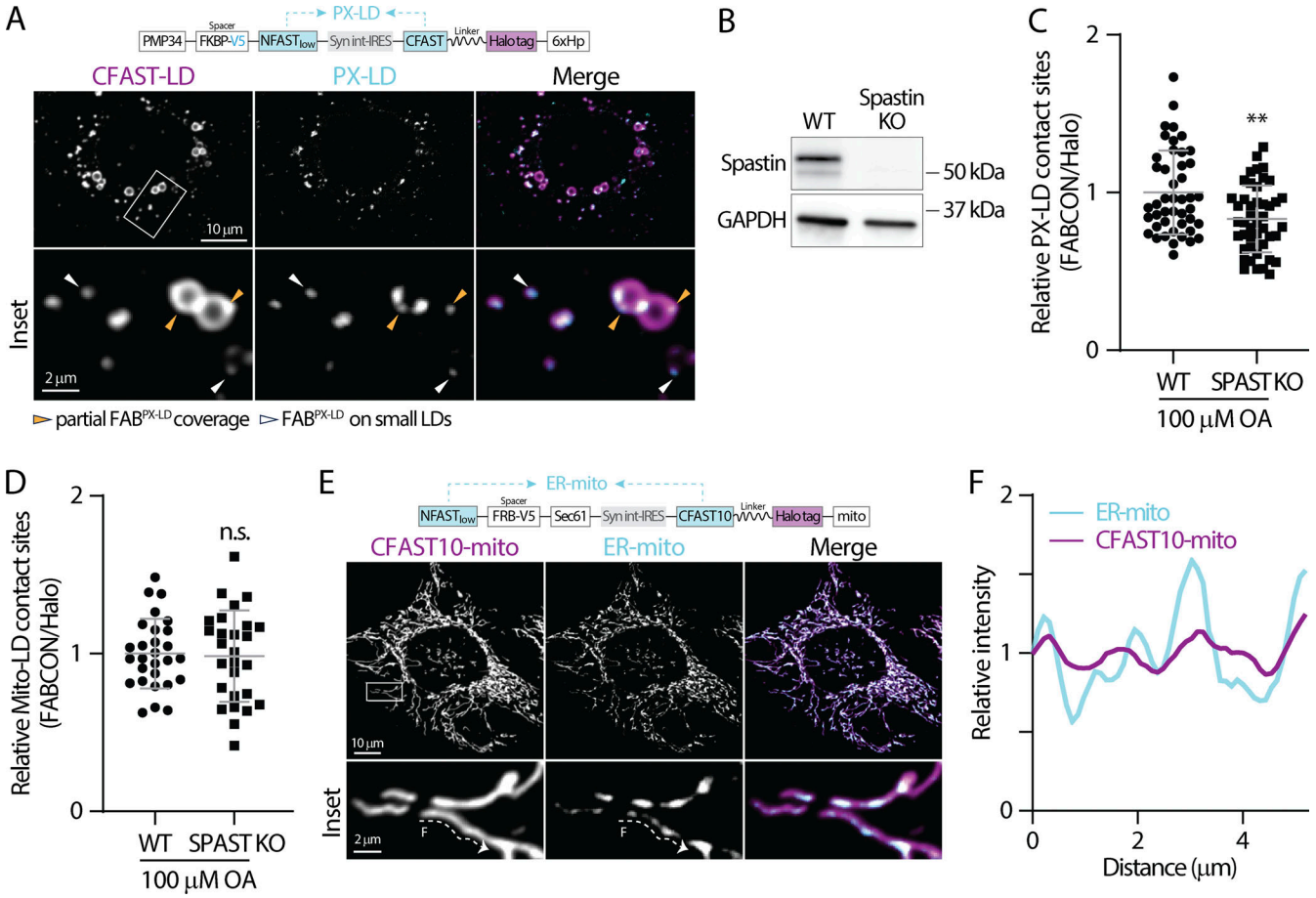

Figure 8. **Detection of PX-LD and ER-mito contact sites using FABCON. (A)** Detection of lipid droplets (LDs) and peroxisome (PX)-LD contact sites in oleic acid (OA)-treated U2OS cells producing FAB$^{PX\text{-}LD}$ (top) monitored via confocal microscopy. Representative maximal intensity projected (MIP) images from three axial slices (~1 µm in total thickness) are shown. **(B)** Spastin (SPAST) protein levels from wild-type (WT) and SPAST knockout (KO) U2OS cells detected by Western blot. **(C)** Relative levels of PX-LD contact sites in WT and SPAST KO U2OS cells. Raw data and mean ± SD are shown (45 cells for each condition from three independent experiments, **P ≤ 0.01, unpaired *t* test, two-tailed). **(D)** Relative levels of mitochondria (mito)-LD contact sites in WT and SPAST KO U2OS cells. Raw data and mean ± SD are shown (26–24 cells from three independent experiments, n.s. = not significant, unpaired *t* test, two-tailed). **(E)** Detection of endoplasmic reticulum (ER)-mito contact sites in HeLa cells producing FAB$^{ER\text{-}mito}$ (top) monitored by confocal microscopy. Representative MIP images from three axial slices (~1 µm in total thickness) are shown. **(F)** Intensity profiles of CFAST10-mito and ER-mito from the dashed line in E. Source data are available for this figure: SourceData F8.

2016) were obtained from the Farese & Walther Lab at the Memorial Sloan Kettering Cancer Center (New York, NY, USA). SUM159 cells were cultured in DMEM/F-12 GlutaMAX (Life Technologies), supplemented with 5% FBS, 1X penicillin/streptomycin solution, 1 µg/ml hydrocortisone (Sigma-Aldrich), 5 µg/ml insulin (Sigma-Aldrich), and 10 mM HEPES (pH 7.0) (Sigma-Aldrich). Transient transfection was performed using TransIT-LT1 (Muris Bio LLC) or Lipofectamine 3000 (Thermo Fisher Scientific) according to manufacturers' instructions for 16–20 h. To knock down PLIN 5, HeLa cells were transfected with 25 nM scramble or PLIN 5 siRNA (Dharmacon) using TransIT-TKO (Mirus Bio LLC) according to the manufacturer's instructions. BODIPY green (Cat# D3922) and far-red (Cat# B3932) were from Thermo Fisher Scientific, MDH (Cat# SM1000a) was purchased from Abcepta, oleic acid–BSA complex, hereafter oleic acid or OA was from Sigma-Aldrich (Cat# O3008) or Cayman Chemicals (Cat# 29557). Triascin C (Cat# T4540), isoproterenol (Cat# I6504), 2DG (Cat# D6134), diaminobenzidine (Cat# D8001), and hydrogen peroxide solution (Cat# H1009) were bought from Sigma-Aldrich.

Generation of Spastin (SPAST) knockout cells

SPAST KO U2OS cells were created using CRISPR-Cas9 technology in the Center for Advanced Genome Engineering at St. Jude Children's Research Hospital. Briefly, 500,000 U2OS cells were transiently transfected with precomplexed ribonuclear proteins (RNPs) consisting of 150 pmol of chemically modified sgRNA (CAGE2489.SPAST.g3 spacer—5′ GACUAAUUUGGUUAU GGCCA-3′, Synthego), 50 pmol of 3X NLS SpCas9 protein (St. Jude Protein Production Core), and 300 ng of pMaxGFP (Lonza) via nucleofection (Lonza, 4D-Nucleofector X-unit) according to the manufacturer's recommended protocol using solution P3 and program CM-104 in a small (20 µl) cuvette. 5 days after nucleofection, cells were single-cell sorted by FACs (St. Jude Flow Cytometry and Cell Sorting Shared Resource) to enrich for GFP+ (transfected) cells into 96-well tissue culture treated plates

containing prewarmed media. GFP signal was expected to be washed out by 2 wk after transfection, and fluorescence microscopy confirmed the absence of GFP signal. Cells were clonally expanded and screened for the desired modification (out-of-frame indels) via targeted deep sequencing using gene-specific primers with partial Illumina adapter overhangs (CAGE2489.SPAST.DS.F—5′-CTACACGACGCTCTTCCGATCTACTCCCCATGAAAGTAGTTTGGG-3′ and CAGE2489.SPAST.DS.R-5′- CAGACGTGTGCTCTTCCGATCTCCTGGACCACATTTTCAATCACT-3′, overhangs shown in uppercase) as previously described (Narina et al., 2023). Next-generation sequencing analysis of clones was performed using CRIS.py (Connelly and Pruett-Miller, 2019). Final clones were authenticated using the PowerPlex Fusion System (Promega), performed at the Hartwell Center for Biotechnology at St. Jude. Final clones were tested negative for mycoplasma by the MycoAlertTMPlus Mycoplasma Detection Kit (Lonza). Knockout was confirmed by Western blotting.

DNA plasmids

FABCON plasmids were generated as follows. We first generated plasmids containing FP- (mApple, mCherry, or Halo) tagged organelle–targeting motifs. FP-1xHp was generated by inserting a 1xHp PCR fragment into an FP-C1 vector using the EcoRI and BamHI restriction sites. FP-6xHp was created by replacing 1xHp in FP-1xHp with a 6xHp gBlock using the BsrGI and BamHI restriction sites. PMP34-FP was generated by inserting a PMP34 PCR fragment into an FP-C1 vector using the NheI and AgeI restriction sites. A CFAST gBlock or an annealing nucleotide and NFAST PCR fragment were inserted into FP-6xHp using the NheI and AgeI restriction sites to generate CFAST-FP-6xHp and NFAST-FP-6xHp, respectively. A linker gBlock was then inserted into CFAST-FP-6xHp using the AgeI restriction site to generate CFAST-linker-FP-6xHp. CFAST-FP-ER was created by replacing 6xHp in CFAST-FP-6xHp with a gBlock containing an ER-targeting motif (Cho et al., 2020) using the SacI and BamHI restriction sites. NFAST-FP-ER, NFAST-FP-Sec61β, and NFAST-FP-mito were created by replacing 6xHp in NFAST-FP-6xHp with gBlocks containing an ER targeting motif, Sec61β, and mitochondria-targeting motif (Benedetti et al., 2020), respectively, using SacI and BamHI. To generate PMP34-FP-NFAST, an NFAST fragment was inserted into PMP34-FP using the Kpn2I and NotI restriction sites. The Halo-TNFa-RUSH construct (Weigel et al., 2021) was used as a backbone to generate bicistronic IRES plasmids. In brief, (5′–3′) NFAST-containing PCR fragments (NheI-NotI digested), a synthetic intron-IRES (NotI-SgsI digested) fragment, and the PCR product of CFAST-linker-Halo-6xHp (SgsI-Acc65I digested) were ligated into the backbone digested with NheI and BsrGI restriction enzymes. To replace FP with spacers in all NFAST-containing halves in IRES plasmids, gBlocks of various spacers (see Fig. S2) were inserted into PCR-amplified backbones omitting FP by InFusion cloning. Lentiviral plasmids were generated by inserting PCR fragments containing coding sequences of NFAST- and CFAST-containing halves flanking IRES element and mApple-6xHp into the lentiviral SJL12 backbone (provided by the St. Jude Vector Core) digested with AgeI and NotI restriction enzymes using InFusion cloning.

APEX2-6xHp was generated by replacing mApple in mApple-6xHp with APEX2 PCR fragments using the NheI and EcoRI restriction sites. mEmerald-Sec61β (#90992) and Halo-TNFα-RUSH (#166901) were obtained from Addgene. All plasmids were confirmed via sequencing. All oligonucleotides (Table S2) and gBlocks were synthesized by Integrated DNA Technologies.

Lentivirus production

Production and titration of lentiviral vectors were performed as described previously (Bauler et al., 2019). Briefly, SJ293TS cells were transfected with the transfer vector and the helper plasmids pCAG-kGP1-1R, pCAG-VSVG, and pCAG4-RTR2 using PEIpro (Polyplus Transfection) and grown in Freestyle 293 Expression media (Thermo Fisher Scientific) at 37°C with 8% CO_2 and shaking at 125 RPM. The next day, Benzonase (Millipore-Sigma) was added to the transfected cells with a final concentration of 6.25 U per ml. Vector supernatants were collected 48 h after transfection, clarified by centrifugation at 330 × *g* for 5 min, and passed through a 0.22-µm sterile filter. Lentiviral vectors containing supernatants were adjusted to 300 mM NaCl, 50 mM Tris pH 8.0 and loaded onto an Acrodisc Mustang Q membrane (Pall Life Sciences) according to the manufacturer's instructions using an Akta Avant chromatography system (GE Healthcare Bio-Sciences). After washing the column with 10 volumes of 300 mM NaCl, 50 mM Tris pH 8.0, viral particles were eluted from the column using 2 M NaCl, Tris pH 8.0. Viral particles were formulated into either X-VIVO 10 or X-VIVO 15 media (Lonza) or phosphate buffered saline containing 1% human serum albumin (Grifols Biologicals) using either a PD10 desalting column (GE Healthcare) or a Vivaflow 50 cassette (Sartorius) according to the manufacturer's instructions to achieve an approximate 50-fold concentration from the starting material. Viral particles were passed through a 0.22 µm sterile filter, aliquoted, and stored at −80°C.

Titration of lentiviral vectors was performed by transducing HOS cells (ATCC CRL-1543) with serially diluted vector preparations in the presence Polybrene (5–8 µg/ml; Millipore Sigma). HOS cells were grown in DMEM (Corning) supplemented with 10% fetal bovine serum (Seradigm) and 2 mM *L*-alanyl-*L*-glutamine (Corning) at 37°C with 5% CO_2. 4 days after transduction, genomic DNA was isolated from transduced HOS cells using a Quick-DNA Miniprep kit (Zymo Research). Vector titers were determined by calculating the ratio between the copies of HIV psi and every two copies of RPP30 via QX200 digital droplet PCR system (Bio-Rad), multiplied by the number of cells transduced and if necessary, multiplied by the dilution factor.

Fluorescence microscopy imaging

General imaging and FRAP

All cells were grown and transiently transfected or infected with lentiviral vectors on Lab-Tek II chambered #1.5 coverglasses (Thermo Fisher Scientific) or MatTek dishes with #1.5 coverslip (MetTek). Prior to imaging, media were replaced with FluoroBrite DMEM (Thermo Fisher Scientific) supplemented with 5% FBS and penicillin/streptomycin and imaged at 37°C. Confocal microscopy was conducted on a custom-built Nikon microscope equipped with a Yokogawa CSU-W1 Spinning Disk unit, XY

galvo scanning module, and Tokai Hit STXG CO_2 incubation system using 60× (CFI APO TIRF, NA 1.49 oil) and 10× (CFI Super Fluor, NA 0.50) objectives. Photobleaching experiments were performed on a Nikon microscope using XY galvo scanning module. Structured illumination microscopy (Gustafsson, 2000) imaging was performed using the Plan Apochromat 63×/1.4 oil objective on a Zeiss ELYRA7 Microscope.

FABCON imaging

Cells were seeded on an eight-well coverglass at a density of 2,000–4,000 cells per well for 24 h followed by FABCON lentivirus infection at a multiplicity of infection (MOI) of 300–500. After 24 h of infection, the infection media was replaced with fresh culture media with an indicated amount of OA. The next day, infected cells were imaged in the presence of 100 nM of Halo ligand JF646, which labels Halo tagged 6xHp on lipid droplets. Then, 3 µM of HBR-2,5DOM (Kumar et al., 2024, *Preprint*; Mineev et al., 2021) was added upon imaging acquisition to label contact sites FABCON, which was imaged with a 488-nm excitation and a 560/50 emission filter. For intensity-based analysis, all images were taken within 10–15 min following fluorogen addition. For lipid droplet (LD) biogenesis and OA withdrawal experiments over 4–8 h, replicated samples were prepared for each time point and data from each sample was obtained within 15-min of dye addition. It is important to note that a maximum of 3 µM fluorogen should be applied to circumvent issues related to enhancing contact site formation.

Lattice light sheet microscopy

U2OS cells were seeded on CS-5R coverslips (Multi Channel Systems) and infected with lentivirus-producing $FAB^{ER\text{-}LD}$. 24 h later, the cells were replenished with fresh DMEM/F12 medium supplemented with 100 µM of oleic acid and incubated overnight. U2OS cells were then imaged in FluoroBrite DMEM with 5% FBS and 100 nM JF646 Halo ligand. Live imaging was acquired with a lattice light sheet microscope (Intelligent Imaging Innovations) operating in single camera mode using a custom emission filter (Chroma ZET488/640m-TRF). Excitation of HBR-2,5DOM and JF646 Halo ligand was achieved using 488-nm and 640-nm lasers (MPB Communications, Inc.) respectively. The desired excitation profile was achieved using a multi-Bessel beam interference pattern (Liu et al., 2023; crop factor ε = −0.15) filtered through an annular mask with inner and outer NA (0.472 and 0.55, respectively) to create a light sheet with empirical propagation length and axial thickness ∼20 and 1.05 µm, respectively, at 488 nm. The propagation length is obtained from an image of a single-Bessel illumination pattern emitted by fluorescein dye solution excited at 488 nm and is the full width at half maximum (FWHM) of the intensity profile along the direction of propagation at the maximum intensity. Note that the length of this single-Bessel beam, created by fully illuminating the annular mask, is a slight underestimate of the multi-Bessel beam produced by the patterned illumination at the same mask. The axial thickness value is obtained from the measured XZ PSF, captured by imaging the emission of a fluorescent 100-nm microbead scanned through the illumination pattern, and is the FWHM of the profile along the axial direction at a pattern maximum. This is well matched to the theoretical values of propagation length (22.5 µm) and axial thickness (1.0 µm) for this pattern at 488 nm (Shi et al., 2022). Emission was detected with a Zeiss 1.1NA using a 20× water immersion detection objective. Volume images were acquired in sample scanning mode with a 0.3-µm step l. Raw images were subsequently deconvolved using a standard Lucy-Richardson algorithm with experimentally acquired lattice light sheet point square functions and resampled to remove the skew orientation introduced by sample scanning.

Cell fixation and immunostaining

All procedures were performed at room temperature and all washing steps were done using Dulbecco's Phosphate-Buffered Saline (DPBS) for 5 min unless otherwise indicated. Cells were rinsed with DPBS and fixed with 4% paraformaldehyde and 0.1% glutaraldehyde in DPBS for 20 min. Fixed cells were quenched with 100 mM glycine in DPBS, washed twice, and permeabilized by 0.3% Triton X-100 in DPBS for 20 min. Permeabilized cells were then blocked with 5% normal donkey or goat serum in DPBS for 1 h followed by incubation with primary antibody (1:200 in dilution; anti-V5 antibody, CST, cat# 13202S; anti-PLIN 2, Abcepta, cat# AP5118c) in DPBS with 1% BSA at 4°C overnight. After three washes, the samples were incubated with an Alexa Fluor Plus 488 conjugated donkey anti-rabbit IgG (1:2,000, cat#A32790; Invitrogen in dilution) for 1 h. The stained samples were washed three times and imaged with confocal microscopy at room temperature.

Image analysis

All image analyses were performed using Fiji (Schindelin et al., 2012) (National Institutes of Health) unless otherwise indicated. All intensity analyses were subjected to background subtraction. To obtain relative intensity profiles, background-subtracted intensity values from different conditions were normalized to that at the first time point or in control groups. To measure the relative contact sites levels, regions of interest (ROIs) of lipid droplets were generated by thresholding CFAST-LD images. These ROIs were then applied to FABCON and CFAST-LD images to obtain their mean gray values. The relative level of contact sites was obtained by normalizing the FABCON mean gray value to that of Halo-6xHp.

For colocalization analysis, the machine learning software ilastik (version 1.4) (Berg et al., 2019) was trained to segment mitochondria (mito), LDs, and peroxisomes (PX) from maximum intensity projected (MIP) images to create binary masks. The masks were then used as the input for JACoP (Just Another Colocalization Plugin) in Fiji to acquire Pearson's correlation coefficient between two organelles.

To measure lipid droplets' number, size, and relative content, HeLa cells transiently transfected with Halo-6xHp (stained with JF646) were fixed after the indicated treatment. Fixed cells were post-stained with BODIPY and confocal images of 6xHp and LDs were acquired. To assess number and size, LDs from 60× confocal images were segmented by ilastik to create binary masks. The LDs' number and average size from each cell were acquired from the masks via "Analyze Particles" in Fiji. For measuring

relative lipid droplet content, background staining of BODIPY throughout the entire cytoplasm from 10× confocal images was the threshold to generate ROIs for single cells using Wand (tracing) tool in Fiji. These ROIs were then applied to 6xHp and lipid droplets images to obtain their mean gray values. Corresponding data from 6xHp and LDs were binned based on 6xHp's values: (i) <20 is considered absence of expression (–), (ii) 20–100 represents low expression (+), and (iii) 200–500 indicates moderate 6xHp expression (++).

COSIMA

COntact SIte MApping (COSIMA) was developed to automate the quantification and plotting of fluorescence intensities at contact sites (i.e., ER-LD, mito-LD) based on the segmentation masks created by ilastik. Original *.nd2 files Z-stacks images were converted into maximum intensity projected *.tif images (MIP) using Fiji. For consistency, the MIP was centered around the structure in focus and included an identical number of slices above and below the focus plane in each channel. 10 MIP images of LDs labeled by CFAST-LD were randomly chosen and manually annotated to be used as a training set for a pixel classifier using ilastik. Three predicted classes were evaluated for each pixel: LD membrane, LD void (center of a LD), and background. The resulting prediction maps (matched to their original images) were further manually annotated and used to create an object classifier using ilastik. This step improved the accuracy of the detection of LD voids by removing false positive objects incorrectly identified by the pixel classifier. The final output was a binary mask of the LD voids and corresponding features saved in *.tif and *.csv format, respectively. Following a critical manual review of the segmentation results on the training dataset, this pipeline was applied to the rest of the images.

COSIMA was created based on the Python programming language and ported to Napari (v 0.4.18, Ahlers, 2023) as a plugin. The software identified each segmented LD void from the input image and created an outline of a defined thickness starting at the edge of the LD void and encompassing the membrane of the LD. The growth of each outline was done sequentially in 1-pixel-wide increments for all the objects present in an image. In the case of adversarial growth between neighboring objects, a dedicated collision module prevented the formation of overlapping outlines by limiting their local expansion. For all datasets, the analyzed area was set to be 5 pixels wide (equivalent to 514 nm) around the void of each LD and was used to measure fluorescence intensities on all channels. Following automated background subtraction, fluorescent intensities were recorded per pixel for each individual layer and averaged radially over the total number of layers analyzed. Final output included measurement tables, LD-specific plots of fluorescence intensities around each object, and annotated images allowing manual review and visual confirmation by the users. This pipeline is available at https://github.com/stjude/cosima.

EM imaging

To investigate mitochondria-LD contact sites, HeLa cells were plated in MatTek dishes (cat# P35G-1.5-10-C) at a density of 3000 cells/dish and infected with lentivirus producing $FAB^{mito\text{-}LD}$. Uninfected and infected HeLa cells were maintained in EMEM medium for an additional 24 h before being supplemented with 100 µM of OA; cells were allowed to grow overnight. For EM imaging, HeLa cells were pre-fixed in a mixture of 2.5% glutaraldehyde, 2% paraformaldehyde, and 0.1 M sucrose in 0.1 M Sorenson's phosphate buffer (PB), pH 7.4 overnight at 4°C. The pre-fixed cells were post-fixed in a mixture of 0.5% OsO_4 and 0.5% $K_4Fe(CN)_6$ in 0.1 M PB, pH 7.4 for 10 min in cold beads. The post-fixed cells were contrasted with 0.5% uranyl acetate overnight at 4°C. Following the contrasting, cells were dehydrated in ascending ethanol series (10, 30, 50%, 70%, 80%, 90%, 95%, and 100%), infiltrated in Spurr's resin (25%, 50%, 75%, and 100%), and embedded in absolute Spurr's resin overnight. Resin-embedded cells were thermally polymerized for 24 h at 70°C. The coverslip under the MatTek glass bottom dish was detached using glass removal fluid and liquid nitrogen. The polymerized cells were sectioned to a 2-µm depth from the block face using a Leica EM ARTOS 3D ultramicrotome (Leica Microsystems) and a diamond knife (DiATOME). The last two sequential ultrathin sections (900 × 900 × 100 nm) were obtained on a formvar/carbon-coated slot grid (2 × 1 mm). The ultrathin sections were post-stained with 1% uranyl acetate.

Contrasted ultrathin sections were observed using a scanning transmission electron microscopy detector at 15 KeV and the high-angle annular dark field imaging mode of a Carl Zeiss Gemini 460 field emission scanning electron microscope. 20 cells per group were randomly selected at 1,000× magnification for an unbiased quantification of contact sites between endoplasmic reticulum and mitochondria. Images at 5,000× and 10,000× per cell were acquired in lipid-rich regions. Reagents and supplies from Electron Microscopy Sciences, unless indicated otherwise.

APEX2-EM validation of 6xHp

To prepare cells for proximity labeling with APEX2 and subsequent electron microscope imaging, 1 × 10^4 U2OS cells were seeded in MatTek dishes (cat# P35G-1.5-10-C) and transfeted with 300 ng of APEX2-6xHp construct. After transfection, U2OS cells were maintained in fresh DMEM/F12 medium supplemented with 100 µM of OA overnight. The U2OS cells were then fixed with 2% glutaraldehyde at room temperature for 5 min, followed by glycine quenching. Subsequently, cells were stained with 1× DAB with 10 mM H_2O_2 for 15 min on ice. Steps to process samples for EM were performed as described previously (Martell et al., 2017). Samples were sectioned at 70 nm on a UC-7 ultramicrotome (Leica) to uncoated copper grids and imaged on a Thermo Fisher Scientific TF20 TEM at 80 keV and images captured with an AMT NanoSprint15 imaging system.

Lipid droplet floatation assay

Lipid droplets were isolated from HepG2 cells following a previously described protocol (Bersuker et al., 2018). Briefly, 1.2 × 10^7 cells (at collection day) were transfected with mApple-1xHp or infected with mApple-6xHp lentiviral particle and incubated with 200 µM OA overnight. Cells were subsequently scraped off the plates into cold PBS buffer and resuspended in 2 ml of HLM buffer (20 mM Tris-HCl, pH 7.4, 1 mM EDTA, pH 8.0) with 1×

complete proteinase inhibitor cocktail (Cat# 11697498001; Sigma-Aldrich). Cell lysis was achieved by passing the cell suspension through 27G needles 30 times, followed by centrifugation at 1,000 × *g* for 10 min at 4°C. Supernatants were mixed with 60% sucrose and overlaid with 5% sucrose and HLM buffer in an SW41 Ti tube (Cat# 344059; Beckman). The gradient was centrifuged at 50,000 × *g* for 60 min and allowed to coast to a stop. After centrifugation, buoyant fractions were separated from the gradients with a tube slicer (Cat# 303811; Beckman). Membrane pellets at the bottom were collected and resuspended in 1 ml of HLM buffer. The protein concentration of each fraction was determined using the bicinchoninic acid (BCA) assay, and an equal amount of protein was loaded into an SDS-PAGE gel for subsequent analysis with Western blot. mApple-tagged proteins were probed with anti-RFP antibody (1:2,000, cat# ab124754; Abcam), perilipin 2 (PLIN 2) was probed with anti-ADFP (Plin2) antibody (1:2,000, cat # AP5811c; Abcepta), and the ER marker VAPA was detected with anti-VAPA antibody (Cat# HPA009174; Sigma-Aldrich).

Western blot

To validate knockout cell lines and cells treated with siRNAs, cells were lysed with IP lysis buffer (Thermo Fisher Scientific) supplemented with 1X protease inhibitor cocktail on ice for 30 min. The cell lysates were centrifuged at 18,000 × *g* for 15 min at 4°C. The supernatant was collected and denatured in Laemmli buffer (with 10% beta-mercaptoethanol) at 95°C for 10 min. Proteins were separated on an SDS-PAGE gel and transferred to a nitrocellulose or PVDF membrane (BIO-RAD). The membrane was blocked with EveryBlot blocking buffer (BIO-RAD) for 1 h and incubated with a primary antibody (1:1,000) overnight. The membrane was then washed with PBST for 10 min three times and incubated with a corresponding secondary antibody (1:2,500). The membrane was then washed again with PBST for 10 min three times before visualization of protein bands. Chemiluminescence was detected using ChemiDoc Imaging System (BIO-RAD). The following antibodies were used in this study: anti-seipin antibody (Cat# H00026580-A02; Abnova), anti-PLIN 5 (Cat# GP31; Progen), anti-VAPA, anti-VAPB (Cat# HPA013144; Sigma-Aldrich), anti-Spastin (Cat# ABN368; Sigma-Aldrich), anti-GAPDH (Cat# 2118; Cell Signaling), goat anti-rabbit IgG-HRP (Cat# 1706515; Bio-Rad), goat anti-mouse IgG-HRP (Cat# 1706516; Bio-Rad), and goat anti-guinea pig IgG-HRP (Cat# A18769; Invitrogen).

Multimodal analysis

A Gaussian mixture model (GMM) was applied to analyze the distribution of mito-LD and ER-LD contact site size. A GMM is an unsupervised machine learning technique used to assign each data point the probability of belonging to a specific cluster. The ER-LD and mito-LD datasets were assumed to comprise two Gaussians two distributions in the GMM analysis. Each data point was assumed to be identically and independently distributed according to the underlying mixture of Gaussian distributions. Each Gaussian distribution in the mixture is composed of three parameters: mean (μ), standard deviation (SD; δ), and mixing probability (p). Parameter estimation was carried out using the expectation-maximization algorithm. The resultant Gaussian distributions were compared with the histogram to visually assess the agreement between the estimated underlying distributions and the observed values of mito-LD and ER-LD. Model fitting evaluation was performed using the Bayesian information criteria (BIC). The corresponding BIC values for the GMM analysis of ER-LD and mito-LD data were 303.95 and 360.89, respectively, suggesting a slightly better fit for the ER-LD data.

Statistical analysis

Data were statistically analyzed using a two-tailed *t* test or one-way analysis of variance with Tukey's multiple comparisons using GraphPad Prism (GraphPad Software). Data distribution was assumed to be normal unless otherwise indicated. A normal distribution test was performed using Prism. *P < 0.05; **P < 0.01; ***P < 0.001; n.s., not significant. Graphs were generated using GraphPad Prism and Adobe Illustrator.

Online supplemental material

Fig. S1 demonstrates the reversibility of the low-affinity split-FAST without detectable fluorescent leakiness. Fig. S2 illustrates the design and validation of FABCON lentiviruses. Fig. S3 shows the number and size of lipid droplets following OA addition and withdrawal. Table S1 lists the organelle-targeting motifs used in this study. Table S2 shows oligonucleotides used in this work.

Data availability

Further information and requests for resources and reagents should be directed to and will be fulfilled by the lead contact, Chi-Lun Chang (Chi-Lun.Chang@stjude.org). Requests will be handled according to the St. Jude Children's Research Hospital policies regarding Material Transfer Agreement and related matters.

Acknowledgments

We would like to thank Dr. Luke Lavis at Janelia Research Campus (Ashburn, VA, USA) for providing JF Halo ligands, Drs. Wade Harper and Jin-mi Heo at Harvard Medical School (Boston, MA, USA) for providing parental and VAP DKO HeLa cells, Drs. Robert Farese, Jr. and Tobias Walther at Memorial Sloan Kettering Cancer Center (New York, NY, USA) for providing parental and Seipin KO SUM159 cells, the Vector Core Lab at St. Jude Children's Research Hospital for generating lentiviral particles, Nathan B. Kurtz for assisting APEX2 experiment, Jonathon Klein and Dr. Shondra M. Pruett-Mille for generating SPAST KO U2OS cells, Dr. David J. Solecki for LLSM consultation, Dr. Danny M. D'Amore for scientific editing, Drs. J. Paul Taylor, Joseph Opferman, and Wyatt Beyers for feedback on the manuscript, and Gunda Johnson, Marquetta Nebo, Jennifer Maglisco, and Monique Payton for administrative and operational assistance.

This work was supported by ALSAC (to C.-L. Chang) and the National Institutes of Health (1DP2GM150192 to C.-L. Chang).

Author contributions: X. Li: Conceptualization, Data curation, Formal analysis, Investigation, Methodology, Validation,

Visualization, Writing—original draft, Writing—review & editing, R. Gamuyao: Conceptualization, Formal analysis, Investigation, Methodology, Validation, Visualization, Writing—original draft, Writing—review & editing, M.-L. Wu: Data curation, Software, Visualization, W.J. Cho: Investigation, Methodology, S.V. King: Methodology, Resources, R.A. Petersen: Methodology, D.R. Stabley: Investigation, Methodology, Resources, Supervision, Writing—review & editing, C. Lindow: Formal analysis, Methodology, L.K. Climer: Investigation, Resources, Writing—review & editing, A. Shirinifard: Data curation, Formal analysis, Methodology, Software, Visualization, Writing—original draft, Writing—review & editing, F. Ferrara: Resources, R.E. Throm: Resources, C.G. Robinson: Data curation, Project administration, Resources, Supervision, Writing—review & editing, Y. Zhou: Formal analysis, Writing—review & editing, A.F. Carisey: Methodology, Resources, A.G. Tebo: Conceptualization, Investigation, Methodology, Resources, Writing—original draft, Writing—review & editing, C.-L. Chang: Conceptualization, Data curation, Formal analysis, Funding acquisition, Investigation, Methodology, Project administration, Resources, Supervision, Validation, Visualization, Writing—original draft, Writing—review & editing.

Disclosures: All authors have completed and submitted the ICMJE Form for Disclosure of Potential Conflicts of Interest. A. Tebo reported a patent to US20220169682A1 pending. No other disclosures were reported.

Submitted: 22 November 2023
Revised: 24 April 2024
Accepted: 31 May 2024

References

Abrisch, R.G., S.C. Gumbin, B.T. Wisniewski, L.L. Lackner, and G.K. Voeltz. 2020. Fission and fusion machineries converge at ER contact sites to regulate mitochondrial morphology. *J. Cell Biol.* 219:e201911122. https://doi.org/10.1083/jcb.201911122

Alford, S.C., Y. Ding, T. Simmen, and R.E. Campbell. 2012. Dimerization-dependent green and yellow fluorescent proteins. *ACS Synth. Biol.* 1: 569–575. https://doi.org/10.1021/sb300050j

Banaszynski, L.A., C.W. Liu, and T.J. Wandless. 2005. Characterization of the FKBP.rapamycin.FRB ternary complex. *J. Am. Chem. Soc.* 127:4715–4721. https://doi.org/10.1021/ja043277y

Bauler, M., J.K. Roberts, C.C. Wu, B. Fan, F. Ferrara, B.H. Yip, S. Diao, Y.I. Kim, J. Moore, S. Zhou, et al. 2019. Production of lentiviral vectors using suspension cells grown in serum-free media. *Mol. Ther. Methods Clin. Dev.* 17:58–68. https://doi.org/10.1016/j.omtm.2019.11.011

Benedetti, L., J.S. Marvin, H. Falahati, A. Guillén-Samander, L.L. Looger, and P. De Camilli. 2020. Optimized Vivid-derived Magnets photodimerizers for subcellular optogenetics in mammalian cells. *Elife*. 9:e63230. https://doi.org/10.7554/eLife.63230

Berg, S., D. Kutra, T. Kroeger, C.N. Straehle, B.X. Kausler, C. Haubold, M. Schiegg, J. Ales, T. Beier, M. Rudy, et al. 2019. ilastik: interactive machine learning for (bio)image analysis. *Nat. Methods*. 16:1226–1232. https://doi.org/10.1038/s41592-019-0582-9

Bersuker, K., C.W.H. Peterson, M. To, S.J. Sahl, V. Savikhin, E.A. Grossman, D.K. Nomura, and J.A. Olzmann. 2018. A proximity labeling strategy provides insights into the composition and dynamics of lipid droplet proteomes. *Dev. Cell*. 44:97–112.e7. https://doi.org/10.1016/j.devcel.2017.11.020

Binns, D., T. Januszewski, Y. Chen, J. Hill, V.S. Markin, Y. Zhao, C. Gilpin, K.D. Chapman, R.G.W. Anderson, and J.M. Goodman. 2006. An intimate collaboration between peroxisomes and lipid bodies. *J. Cell Biol.* 173: 719–731. https://doi.org/10.1083/jcb.200511125

Bishop, A., M. Kamoshita, J.B. Passmore, C. Hacker, T.A. Schrader, H.R. Waterham, J.L. Costello, and M. Schrader. 2019. Fluorescent tools to analyze peroxisome–endoplasmic reticulum interactions in mammalian cells. *Contact*. 2:2515256419848641. https://doi.org/10.1177/2515256419848641

Brown, J. 1962. Effects of 2-deoxyglucose on carbohydrate metablism: Review of the literature and studies in the rat. *Metabolism*. 11:1098–1112.

Chang, C.L., A.V. Weigel, M.S. Ioannou, H.A. Pasolli, C.S. Xu, D.R. Peale, G. Shtengel, M. Freeman, H.F. Hess, C. Blackstone, and J. Lippincott-Schwartz. 2019. Spastin tethers lipid droplets to peroxisomes and directs fatty acid trafficking through ESCRT-III. *J. Cell Biol.* 218:2583–2599. https://doi.org/10.1083/jcb.201902061

Cho, K.F., T.C. Branon, S. Rajeev, T. Svinkina, N.D. Udeshi, T. Thoudam, C. Kwak, H.W. Rhee, I.K. Lee, S.A. Carr, and A.Y. Ting. 2020. Split-TurboID enables contact-dependent proximity labeling in cells. *Proc. Natl. Acad. Sci. USA*. 117:12143–12154. https://doi.org/10.1073/pnas.1919528117

Choudhary, V., and R. Schneiter. 2020. Lipid droplet biogenesis from specialized ER subdomains. *Microb. Cell*. 7:218–221. https://doi.org/10.15698/mic2020.08.727

Cieri, D., M. Vicario, M. Giacomello, F. Vallese, R. Filadi, T. Wagner, T. Pozzan, P. Pizzo, L. Scorrano, M. Brini, and T. Calì. 2018. SPLICS: A split green fluorescent protein-based contact site sensor for narrow and wide heterotypic organelle juxtaposition. *Cell Death Differ.* 25:1131–1145. https://doi.org/10.1038/s41418-017-0033-z

Connelly, J.P., and S.M. Pruett-Miller. 2019. CRIS.py: A versatile and high-throughput analysis program for CRISPR-based Genome editing. *Sci. Rep.* 9:4194. https://doi.org/10.1038/s41598-019-40896-w

Csordás, G., P. Várnai, T. Golenár, S. Roy, G. Purkins, T.G. Schneider, T. Balla, and G. Hajnóczky. 2010. Imaging interorganelle contacts and local calcium dynamics at the ER-mitochondrial interface. *Mol. Cell*. 39: 121–132. https://doi.org/10.1016/j.molcel.2010.06.029

de Vries, J.E., M.M. Vork, T.H. Roemen, Y.F. de Jong, J.P. Cleutjens, G.J. van der Vusse, and M. van Bilsen. 1997. Saturated but not mono-unsaturated fatty acids induce apoptotic cell death in neonatal rat ventricular myocytes. *J. Lipid Res.* 38:1384–1394. https://doi.org/10.1016/S0022-2275(20)37421-6

Eisenberg-Bord, M., N. Shai, M. Schuldiner, and M. Bohnert. 2016. A tether is a tether is a tether: Tethering at membrane contact sites. *Dev. Cell*. 39: 395–409. https://doi.org/10.1016/j.devcel.2016.10.022

Fei, W., H. Li, G. Shui, T.S. Kapterian, C. Bielby, X. Du, A.J. Brown, P. Li, M.R. Wenk, P. Liu, and H. Yang. 2011. Molecular characterization of seipin and its mutants: Implications for seipin in triacylglycerol synthesis. *J. Lipid Res.* 52:2136–2147. https://doi.org/10.1194/jlr.M017566

Fei, W., G. Shui, B. Gaeta, X. Du, L. Kuerschner, P. Li, A.J. Brown, M.R. Wenk, R.G. Parton, and H. Yang. 2008. Fld1p, a functional homologue of human seipin, regulates the size of lipid droplets in yeast. *J. Cell Biol.* 180: 473–482. https://doi.org/10.1083/jcb.200711136

Fujimoto, Y., H. Itabe, T. Kinoshita, K.J. Homma, J. Onoduka, M. Mori, S. Yamaguchi, M. Makita, Y. Higashi, A. Yamashita, and T. Takano. 2007. Involvement of ACSL in local synthesis of neutral lipids in cytoplasmic lipid droplets in human hepatocyte HuH7. *J. Lipid Res.* 48:1280–1292. https://doi.org/10.1194/jlr.M700050-JLR200

Gallardo-Montejano, V.I., G. Saxena, C.M. Kusminski, C. Yang, J.L. McAfee, L. Hahner, K. Hoch, W. Dubinsky, V.A. Narkar, and P.E. Bickel. 2016. Nuclear Perilipin 5 integrates lipid droplet lipolysis with PGC-1α/SIRT1-dependent transcriptional regulation of mitochondrial function. *Nat. Commun.* 7:12723. https://doi.org/10.1038/ncomms12723

Gatta, A.T., and T.P. Levine. 2017. Piecing together the patchwork of contact sites. *Trends Cell Biol.* 27:214–229. https://doi.org/10.1016/j.tcb.2016.08.010

Greenfield, J.J., and S. High. 1999. The Sec61 complex is located in both the ER and the ER-Golgi intermediate compartment. *J. Cell Sci.* 112:1477–1486. https://doi.org/10.1242/jcs.112.10.1477

Gustafsson, M.G. 2000. Surpassing the lateral resolution limit by a factor of two using structured illumination microscopy. *J. Microsc.* 198:82–87. https://doi.org/10.1046/j.1365-2818.2000.00710.x

Harmon, M., P. Larkman, G. Hardingham, M. Jackson, and P. Skehel. 2017. A Bi-fluorescence complementation system to detect associations between the Endoplasmic reticulum and mitochondria. *Sci. Rep.* 7:17467. https://doi.org/10.1038/s41598-017-17278-1

Hartman, E.J., S. Omura, and M. Laposata. 1989. Triacsin C: A differential inhibitor of arachidonoyl-CoA synthetase and nonspecific long chain acyl-CoA synthetase. *Prostaglandins*. 37:655–671. https://doi.org/10.1016/0090-6980(89)90103-2

Henne, W.M., M.L. Reese, and J.M. Goodman. 2018. The assembly of lipid droplets and their roles in challenged cells. *EMBO J.* 37:e98947. https://doi.org/10.15252/embj.201898947

Heo, J.M., A. Ordureau, J.A. Paulo, J. Rinehart, and J.W. Harper. 2015. The PINK1-PARKIN mitochondrial ubiquitylation pathway drives a program of OPTN/NDP52 recruitment and TBK1 activation to promote mitophagy. *Mol. Cell.* 60:7–20. https://doi.org/10.1016/j.molcel.2015.08.016

Herker, E., G. Vieyres, M. Beller, N. Krahmer, and M. Bohnert. 2021. Lipid droplet contact sites in Health and disease. *Trends Cell Biol.* 31:345–358. https://doi.org/10.1016/j.tcb.2021.01.004

Hugenroth, M., and M. Bohnert. 2020. Come a little bit closer! Lipid droplet-ER contact sites are getting crowded. *Biochim. Biophys. Acta Mol. Cell Res.* 1867:118603. https://doi.org/10.1016/j.bbamcr.2019.118603

Huppertz, M.-C., J. Wilhelm, V. Grenier, M.W. Schneider, T. Falt, N. Porzberg, D. Hausmann, D.C. Hoffmann, L. Hai, M. Tarnawski, et al. 2024. Recording physiological history of cells with chemical labeling. *Science.* 383:890–897. https://doi.org/10.1126/science.adg0812

Ishikawa, H., F. Meng, N. Kondo, A. Iwamoto, and Z. Matsuda. 2012. Generation of a dual-functional split-reporter protein for monitoring membrane fusion using self-associating split GFP. *Protein Eng. Des. Sel.* 25:813–820. https://doi.org/10.1093/protein/gzs051

Jumper, J., R. Evans, A. Pritzel, T. Green, M. Figurnov, O. Ronneberger, K. Tunyasuvunakool, R. Bates, A. Žídek, A. Potapenko, et al. 2021. Highly accurate protein structure prediction with AlphaFold. *Nature.* 596: 583–589. https://doi.org/10.1038/s41586-021-03819-2

Kakimoto, Y., S. Tashiro, R. Kojima, Y. Morozumi, T. Endo, and Y. Tamura. 2018. Visualizing multiple inter-organelle contact sites using the organelle-targeted split-GFP system. *Sci. Rep.* 8:6175. https://doi.org/10.1038/s41598-018-24466-0

Kompa, J., J. Bruins, M. Glogger, J. Wilhelm, M.S. Frei, M. Tarnawski, E. D'Este, M. Heilemann, J. Hiblot, and K. Johnsson. 2023. Exchangeable HaloTag ligands for super-resolution fluorescence microscopy. *J. Am. Chem. Soc.* 145:3075–3083. https://doi.org/10.1021/jacs.2c11969

Kong, J., Y. Ji, Y.G. Jeon, J.S. Han, K.H. Han, J.H. Lee, G. Lee, H. Jang, S.S. Choe, M. Baes, and J.B. Kim. 2020. Spatiotemporal contact between peroxisomes and lipid droplets regulates fasting-induced lipolysis via PEX5. *Nat. Commun.* 11:578. https://doi.org/10.1038/s41467-019-14176-0

Kory, N., A.R. Thiam, R.V. Farese Jr., and T.C. Walther. 2015. Protein crowding is a determinant of lipid droplet protein composition. *Dev. Cell.* 34:351–363. https://doi.org/10.1016/j.devcel.2015.06.007

Kumar, N., M. Leonzino, W. Hancock-Cerutti, F.A. Horenkamp, P. Li, J.A. Lees, H. Wheeler, K.M. Reinisch, and P. De Camilli. 2018. VPS13A and VPS13C are lipid transport proteins differentially localized at ER contact sites. *J. Cell Biol.* 217:3625–3639. https://doi.org/10.1083/jcb.201807019

Kumar, P., A. Gutu, A. Waring, T.A. Brown, L.D. Lavis, and A.G. Tebo. 2024. Transforming chemigenetic bimolecular fluorescence complementation systems into chemical dimerizers using chemistry. *bioRxiv*. https://doi.org/10.1101/2023.12.30.573644 (Preprint posted December 30, 2023).

Lam, S.S., J.D. Martell, K.J. Kamer, T.J. Deerinck, M.H. Ellisman, V.K. Mootha, and A.Y. Ting. 2015. Directed evolution of APEX2 for electron microscopy and proximity labeling. *Nat. Methods.* 12:51–54. https://doi.org/10.1038/nmeth.3179

Lee, J.E., P.I. Cathey, H. Wu, R. Parker, and G.K. Voeltz. 2020. Endoplasmic reticulum contact sites regulate the dynamics of membraneless organelles. *Science.* 367:eaay7108. https://doi.org/10.1126/science.aay7108

Liu, G., X. Ruan, D.E. Milkie, F. Görlitz, M. Mueller, W. Hercule, A. Killilea, E. Betzig, and S. Upadhyayula. 2023. Characterization, comparison, and optimization of lattice light sheets. *Sci. Adv.* 9:eade6623. https://doi.org/10.1126/sciadv.ade6623

Martell, J.D., T.J. Deerinck, S.S. Lam, M.H. Ellisman, and A.Y. Ting. 2017. Electron microscopy using the genetically encoded APEX2 tag in cultured mammalian cells. *Nat. Protoc.* 12:1792–1816. https://doi.org/10.1038/nprot.2017.065

Mineev, K.S., S.A. Goncharuk, M.V. Goncharuk, N.V. Povarova, A.I. Sokolov, N.S. Baleeva, A.Y. Smirnov, I.N. Myasnyanko, D.A. Ruchkin, S. Bukhdruker, et al. 2021. NanoFAST: Structure-based design of a small fluorogen-activating protein with only 98 amino acids. *Chem. Sci.* 12: 6719–6725. https://doi.org/10.1039/D1SC01454D

Miner, G.E., S.Y. Smith, W.K. Showalter, C.M. So, J.V. Ragusa, A.E. Powers, M.C. Zanellati, C.H. Hsu, M.F. Marchan, and S. Cohen. 2024. Contact-FP: A dimerization-dependent fluorescent protein toolkit for visualizing membrane contact site dynamics. *Contact.* 7:25152564241228911. https://doi.org/10.1177/25152564241228911

Miner, G.E., C.M. So, W. Edwards, J.V. Ragusa, J.T. Wine, D. Wong Gutierrez, M.V. Airola, L.E. Herring, R.A. Coleman, E.L. Klett, and S. Cohen. 2023. PLIN5 interacts with FATP4 at membrane contact sites to promote lipid droplet-to-mitochondria fatty acid transport. *Dev. Cell.* 58:1250–1265.e6. https://doi.org/10.1016/j.devcel.2023.05.006

Minner-Meinen, R., J.N. Weber, A. Albrecht, R. Matis, M. Behnecke, C. Tietge, S. Frank, J. Schulze, H. Buschmann, P.J. Walla, et al. 2021. Split-HaloTag imaging assay for sophisticated microscopy of protein-protein interactions in planta. *Plant Commun.* 2:100212. https://doi.org/10.1016/j.xplc.2021.100212

Murphy, S.E., and T.P. Levine. 2016. VAP, a versatile access point for the endoplasmic reticulum: Review and analysis of FFAT-like motifs in the VAPome. *Biochim. Biophys. Acta.* 1861:952–961. https://doi.org/10.1016/j.bbalip.2016.02.009

Najt, C.P., S. Adhikari, T.D. Heden, W. Cui, E.R. Gansemer, A.J. Rauckhorst, T.W. Markowski, L. Higgins, E.W. Kerr, M.D. Boyum, et al. 2023. Organelle interactions compartmentalize hepatic fatty acid trafficking and metabolism. *Cell Rep.* 42:112435. https://doi.org/10.1016/j.celrep.2023.112435

Nakajima, S., M. Gotoh, K. Fukasawa, K. Murakami-Murofushi, and H. Kunugi. 2019. Oleic acid is a potent inducer for lipid droplet accumulation through its esterification to glycerol by diacylglycerol acyltransferase in primary cortical astrocytes. *Brain Res.* 1725:146484. https://doi.org/10.1016/j.brainres.2019.146484

Naon, D., M. Zaninello, M. Giacomello, T. Varanita, F. Grespi, S. Lakshminaranayan, A. Serafini, M. Semenzato, S. Herkenne, M.I. Hernández-Alvarez, et al. 2016. Critical reappraisal confirms that Mitofusin 2 is an endoplasmic reticulum-mitochondria tether. *Proc. Natl. Acad. Sci. USA.* 113:11249–11254. https://doi.org/10.1073/pnas.1606786113

Narina, S., J.P. Connelly, and S.M. Pruett-Miller. 2023. High-Throughput analysis of CRISPR-cas9 editing outcomes in cell and animal models using CRIS.py. *Methods Mol. Biol.* 2631:155–182. https://doi.org/10.1007/978-1-0716-2990-1_6

Nettebrock, N.T., and M. Bohnert. 2020. Born this way: Biogenesis of lipid droplets from specialized ER subdomains. *Biochim. Biophys. Acta Mol. Cell Biol. Lipids.* 1865:158448. https://doi.org/10.1016/j.bbalip.2019.04.008

Olzmann, J.A., and P. Carvalho. 2019. Dynamics and functions of lipid droplets. *Nat. Rev. Mol. Cell Biol.* 20:137–155. https://doi.org/10.1038/s41580-018-0085-z

Ouyang, Q., Q. Chen, S. Ke, L. Ding, X. Yang, P. Rong, W. Feng, Y. Cao, Q. Wang, M. Li, et al. 2023. Rab8a as a mitochondrial receptor for lipid droplets in skeletal muscle. *Dev. Cell.* 58:289–305.e6. https://doi.org/10.1016/j.devcel.2023.01.007

Palade, G.E. 1952. A study of fixation for electron microscopy. *J. Exp. Med.* 95: 285–298. https://doi.org/10.1084/jem.95.3.285

Plamont, M.A., E. Billon-Denis, S. Maurin, C. Gauron, F.M. Pimenta, C.G. Specht, J. Shi, J. Quérard, B. Pan, J. Rossignol, et al. 2016. Small fluorescence-activating and absorption-shifting tag for tunable protein imaging in vivo. *Proc. Natl. Acad. Sci. USA.* 113:497–502. https://doi.org/10.1073/pnas.1513094113

Porter, K.R., and G.E. Palade. 1957. Studies on the endoplasmic reticulum. III. Its form and distribution in striated muscle cells. *J. Biophys. Biochem. Cytol.* 3:269–300. https://doi.org/10.1083/jcb.3.2.269

Poteser, M., G. Leitinger, E. Pritz, D. Platzer, I. Frischauf, C. Romanin, and K. Groschner. 2016. Live-cell imaging of ER-PM contact architecture by a novel TIRFM approach reveals extension of junctions in response to store-operated Ca^{2+}-entry. *Sci. Rep.* 6:35656. https://doi.org/10.1038/srep35656

Prinz, W.A., A. Toulmay, and T. Balla. 2020. The functional universe of membrane contact sites. *Nat. Rev. Mol. Cell Biol.* 21:7–24. https://doi.org/10.1038/s41580-019-0180-9

Rakotoarison, L.-M., A.G. Tebo, D. Böken, S. Board, L. El Hajji, and A. Gautier. 2024. Improving split reporters of protein-protein interactions through orthology-based protein engineering. *ACS Chem. Biol.* 19:428–441. https://doi.org/10.1021/acschembio.3c00631

Rambold, A.S., S. Cohen, and J. Lippincott-Schwartz. 2015. Fatty acid trafficking in starved cells: Regulation by lipid droplet lipolysis, autophagy, and mitochondrial fusion dynamics. *Dev. Cell.* 32:678–692. https://doi.org/10.1016/j.devcel.2015.01.029

Renne, M.F., and H. Hariri. 2021. Lipid droplet-organelle contact sites as hubs for fatty acid metabolism, trafficking, and metabolic channeling. *Front. Cell Dev. Biol.* 9:726261. https://doi.org/10.3389/fcell.2021.726261

Roberts, M.A., K.K. Deol, A.J. Mathiowetz, M. Lange, D.E. Leto, J. Stevenson, S.H. Hashemi, D.W. Morgens, E. Easter, K. Heydari, et al. 2023. Parallel CRISPR-Cas9 screens identify mechanisms of PLIN2 and lipid droplet regulation. *Dev. Cell.* 58:1782–1800.e1710. https://doi.org/10.1016/j.devcel.2023.07.001

Romei, M.G., and S.G. Boxer. 2019. Split green fluorescent proteins: Scope, limitations, and outlook. *Annu. Rev. Biophys.* 48:19–44. https://doi.org/10.1146/annurev-biophys-051013-022846

Sadh, K., P. Rai, and R. Mallik. 2017. Feeding-fasting dependent recruitment of membrane microdomain proteins to lipid droplets purified from the liver. *PLoS One*. 12:e0183022. https://doi.org/10.1371/journal.pone.0183022

Salo, V.T., I. Belevich, S. Li, L. Karhinen, H. Vihinen, C. Vigouroux, J. Magré, C. Thiele, M. Hölttä-Vuori, E. Jokitalo, and E. Ikonen. 2016. Seipin regulates ER-lipid droplet contacts and cargo delivery. *EMBO J.* 35: 2699–2716. https://doi.org/10.15252/embj.201695170

Salo, V.T., S. Li, H. Vihinen, M. Hölttä-Vuori, A. Szkalisity, P. Horvath, I. Belevich, J. Peränen, C. Thiele, P. Somerharju, et al. 2019. Seipin facilitates triglyceride flow to lipid droplet and counteracts droplet ripening via endoplasmic reticulum contact. *Dev. Cell*. 50:478–493.e9. https://doi.org/10.1016/j.devcel.2019.05.016

Schindelin, J., I. Arganda-Carreras, E. Frise, V. Kaynig, M. Longair, T. Pietzsch, S. Preibisch, C. Rueden, S. Saalfeld, B. Schmid, et al. 2012. Fiji: An open-source platform for biological-image analysis. *Nat. Methods*. 9: 676–682. https://doi.org/10.1038/nmeth.2019

Scorrano, L., M.A. De Matteis, S. Emr, F. Giordano, G. Hajnóczky, B. Kornmann, L.L. Lackner, T.P. Levine, L. Pellegrini, K. Reinisch, et al. 2019. Coming together to define membrane contact sites. *Nat. Commun.* 10: 1287. https://doi.org/10.1038/s41467-019-09253-3

Shai, N., E. Yifrach, C.W.T. van Roermund, N. Cohen, and C. Bibi, L. Ijlst, L. Cavellini, J. Meurisse, R. Schuster, L. Zada, et al. 2018. Systematic mapping of contact sites reveals tethers and a function for the peroxisome-mitochondria contact. *Nat. Commun.* 9:1761. https://doi.org/10.1038/s41467-018-03957-8

Shao, S., H. Zhang, Y. Zeng, Y. Li, C. Sun, and Y. Sun. 2021. TagBiFC technique allows long-term single-molecule tracking of protein-protein interactions in living cells. *Commun. Biol.* 4:378. https://doi.org/10.1038/s42003-021-01896-7

Shi, Y., T.A. Daugird, and W.R. Legant. 2022. A quantitative analysis of various patterns applied in lattice light sheet microscopy. *Nat. Commun.* 13:4607. https://doi.org/10.1038/s41467-022-32341-w

Shiratori, R., K. Furuichi, M. Yamaguchi, N. Miyazaki, H. Aoki, H. Chibana, K. Ito, and S. Aoki. 2019. Glycolytic suppression dramatically changes the intracellular metabolic profile of multiple cancer cell lines in a mitochondrial metabolism-dependent manner. *Sci. Rep.* 9:18699. https://doi.org/10.1038/s41598-019-55296-3

Sottnik, J.L., J.C. Lori, B.J. Rose, and D.H. Thamm. 2011. Glycolysis inhibition by 2-deoxy-D-glucose reverts the metastatic phenotype in vitro and in vivo. *Clin. Exp. Metastasis*. 28:865–875. https://doi.org/10.1007/s10585-011-9417-5

Talari, N.K., U. Mattam, N.K. Meher, A.K. Paripati, K. Mahadev, T. Krishnamoorthy, and N.B.V. Sepuri. 2023. Lipid-droplet associated mitochondria promote fatty-acid oxidation through a distinct bioenergetic pattern in male Wistar rats. *Nat. Commun.* 14:766. https://doi.org/10.1038/s41467-023-36432-0

Tashiro, S., Y. Kakimoto, M. Shinmyo, S. Fujimoto, and Y. Tamura. 2020. Improved split-GFP systems for visualizing organelle contact sites in yeast and human cells. *Front. Cell Dev. Biol.* 8:571388. https://doi.org/10.3389/fcell.2020.571388

Tebo, A.G., and A. Gautier. 2019. A split fluorescent reporter with rapid and reversible complementation. *Nat. Commun.* 10:2822. https://doi.org/10.1038/s41467-019-10855-0

Tebo, A.G., B. Moeyaert, M. Thauvin, I. Carlon-Andres, D. Böken, M. Volovitch, S. Padilla-Parra, P. Dedecker, S. Vriz, and A. Gautier. 2021. Orthogonal fluorescent chemogenetic reporters for multicolor imaging. *Nat. Chem. Biol.* 17:30–38. https://doi.org/10.1038/s41589-020-0611-0

To, T.L., Q. Zhang, and X. Shu. 2016. Structure-guided design of a reversible fluorogenic reporter of protein-protein interactions. *Protein Sci.* 25: 748–753. https://doi.org/10.1002/pro.2866

Tomoda, H., K. Igarashi, and S. Omura. 1987. Inhibition of acyl-CoA synthetase by triacsins. *Biochim. Biophys. Acta*. 921:595–598. https://doi.org/10.1016/0005-2760(87)90088-9

Valm, A.M., S. Cohen, W.R. Legant, J. Melunis, U. Hershberg, E. Wait, A.R. Cohen, M.W. Davidson, E. Betzig, and J. Lippincott-Schwartz. 2017. Applying systems-level spectral imaging and analysis to reveal the organelle interactome. *Nature*. 546:162–167. https://doi.org/10.1038/nature22369

Venditti, R., L.R. Rega, M.C. Masone, M. Santoro, E. Polishchuk, D. Sarnataro, S. Paladino, S. D'Auria, A. Varriale, V.M. Olkkonen, et al. 2019. Molecular determinants of ER-Golgi contacts identified through a new FRET-FLIM system. *J. Cell Biol.* 218:1055–1065. https://doi.org/10.1083/jcb.201812020

Walther, T.C., J. Chung, and R.V. Farese Jr. 2017. Lipid droplet biogenesis. *Annu. Rev. Cell Dev. Biol.* 33:491–510. https://doi.org/10.1146/annurev-cellbio-100616-060608

Wang, H., M. Becuwe, B.E. Housden, C. Chitraju, A.J. Porras, M.M. Graham, X.N. Liu, A.R. Thiam, D.B. Savage, A.K. Agarwal, et al. 2016. Seipin is required for converting nascent to mature lipid droplets. *Elife*. 5:e16582. https://doi.org/10.7554/eLife.16582

Wang, H., U. Sreenivasan, H. Hu, A. Saladino, B.M. Polster, L.M. Lund, D.W. Gong, W.C. Stanley, and C. Sztalryd. 2011. Perilipin 5, a lipid droplet-associated protein, provides physical and metabolic linkage to mitochondria. *J. Lipid Res.* 52:2159–2168. https://doi.org/10.1194/jlr.M017939

Wang, J., N. Fang, J. Xiong, Y. Du, Y. Cao, and W.K. Ji. 2021. An ESCRT-dependent step in fatty acid transfer from lipid droplets to mitochondria through VPS13D-TSG101 interactions. *Nat. Commun.* 12:1252. https://doi.org/10.1038/s41467-021-21525-5

Weigel, A.V., C.L. Chang, G. Shtengel, C.S. Xu, D.P. Hoffman, M. Freeman, N. Iyer, J. Aaron, S. Khuon, J. Bogovic, et al. 2021. ER-to-Golgi protein delivery through an interwoven, tubular network extending from ER. *Cell*. 184:2412–2429.e16. https://doi.org/10.1016/j.cell.2021.03.035

Wong, Y.C., D. Ysselstein, and D. Krainc. 2018. Mitochondria-lysosome contacts regulate mitochondrial fission via RAB7 GTP hydrolysis. *Nature*. 554:382–386. https://doi.org/10.1038/nature25486

Supplemental material

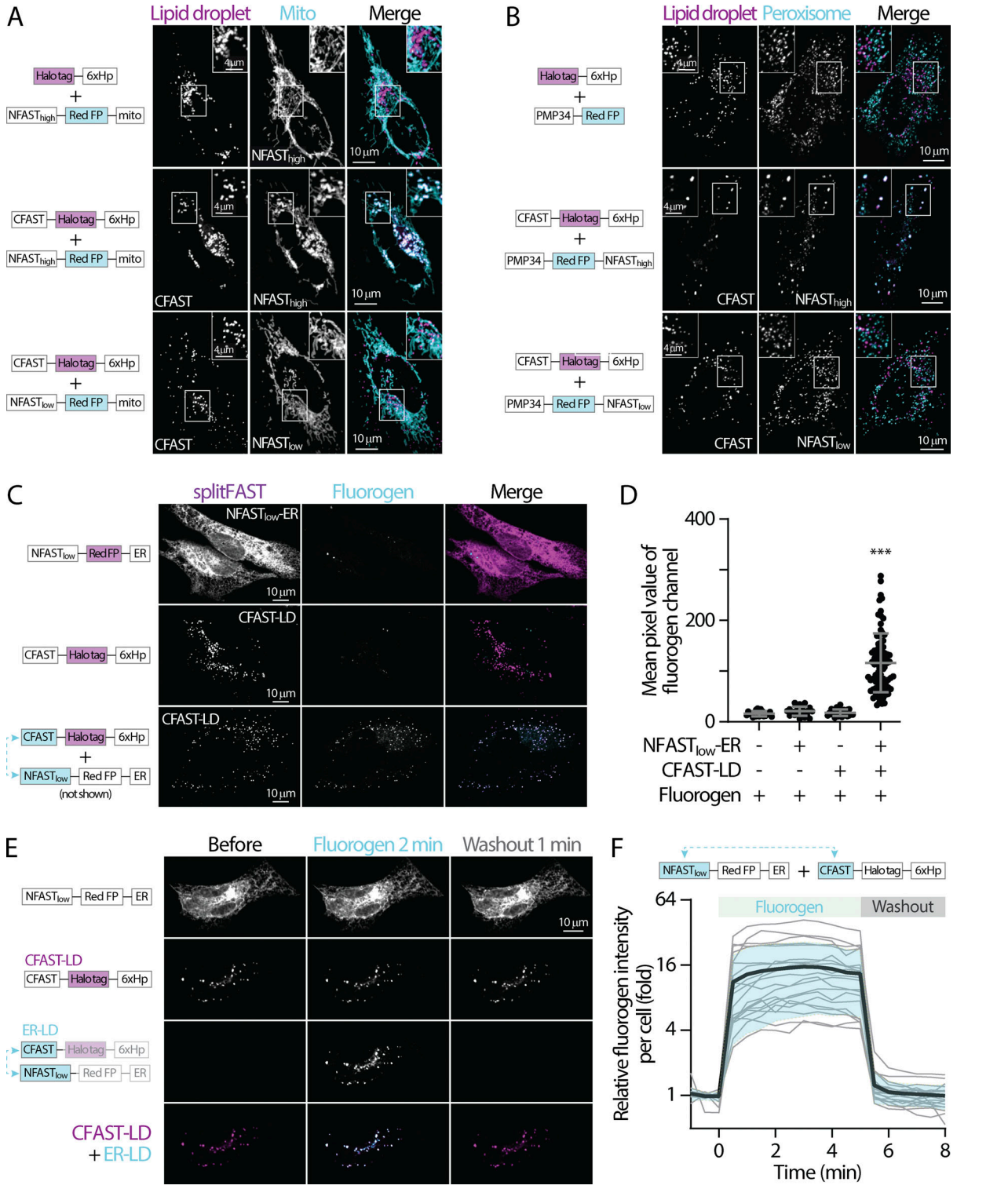

Figure S1. **splitFAST remains reversible at organelle contact sites without detectable fluorescence leakiness. (A)** Distribution of lipid droplets (LDs) and mitochondria (mito) in oleic acid (OA)-treated HeLa cells overexpressing Halo-6xHp and NFAST$_{high}$-mApple-mito, CFAST-Halo-6xHp and NFAST$_{high}$-mApple-mito, or CFAST-Halo-6xHp and NFAST$_{low}$-mApple-mito monitored using confocal microscopy. Maximal intensity projected images from six axial slices (1.8 µm in total thickness) are shown. **(B)** Distribution of LDs and peroxisomes in OA-treated HeLa cells overexpressing Halo-6xHp and PMP34-mApple, CFAST-Halo-6xHp and PMP34-mApple-NFAST$_{high}$, or CFAST-Halo-6xHp and PMP34-mApple-NFAST$_{low}$. **(C)** Confocal images of HeLa cells expressing NFAST$_{low}$-mApple-ER (top), CFAST-Halo-6xHp (middle), and NFAST$_{low}$-mApple-ER plus CFAST-Halo-6xHp (bottom) in the presence of HBR-2,5DOM. **(D)** Quantification of fluorogen intensity of C and in control HeLa cells. Raw data and mean ± SD are shown (22–82 cells). ***P ≤ 0.001, assessed by one-way ANOVA. **(E)** Distribution NFAST$_{low}$-mApple-ER, CFAST-Halo-6xHp, and endoplasmic reticulum (ER)-LD contact site labeled in Hela cells in the absence, 2 min after the addition, and 1 min after the washout of HBR-2,5DOM. **(F)** Relative fluorogen intensity described in E following HBR-2,5DOM addition and washout monitored by confocal microscopy. Raw data (gray traces) and mean (bold black trace) ± SD (shaded blue) are shown (19 or 20 cells).

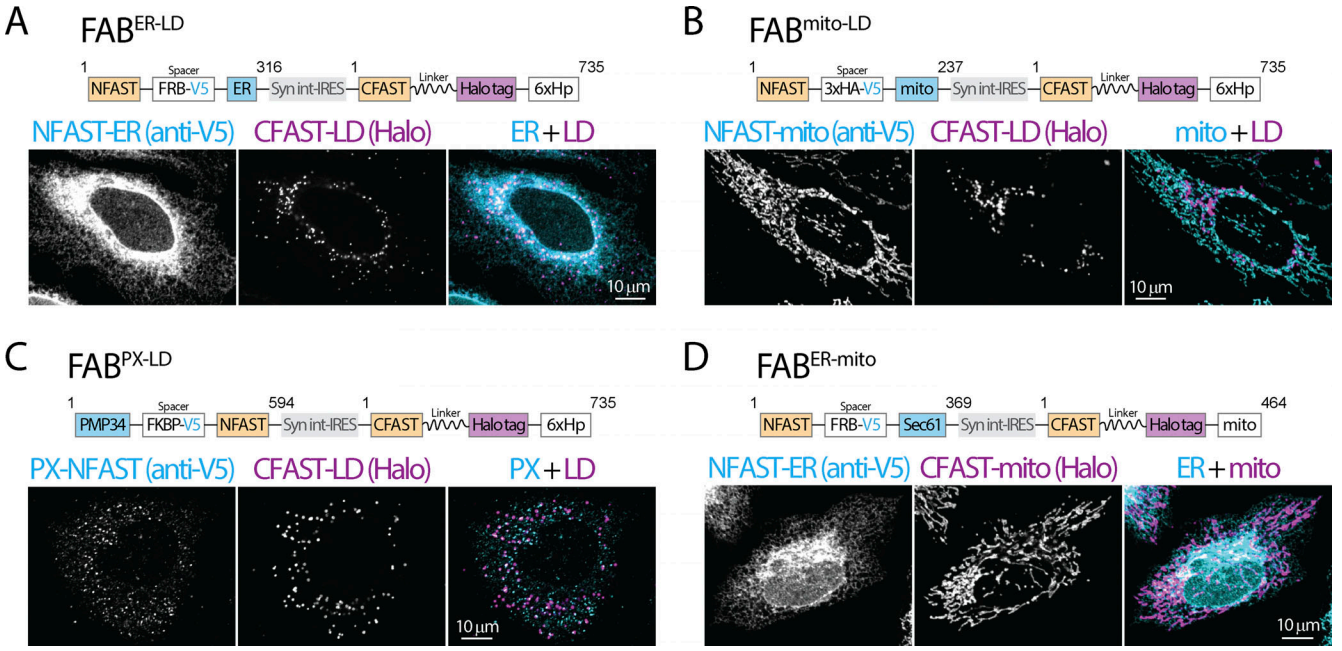

Figure S2. **Diagram and validation of FABCON lentiviruses. (A–D)** Diagram (top) and organelle distribution of cognate FABCON halves (bottom) of FAB$^{ER\text{-}LD}$ (A), FAB$^{mito\text{-}LD}$ (B), FAB$^{PX\text{-}LD}$ (C), and FAB$^{ER\text{-}mito}$ (D) monitored by confocal microscopy. NFAST fused organelle marker were immunostained with anti-V5 antibody. Maximal intensity projected images from three axial slices (~1 μm in total thickness) are shown. Numbers of amino acids are indicated. Syn int-IRES, synthetic intron-internal ribosome entry site.

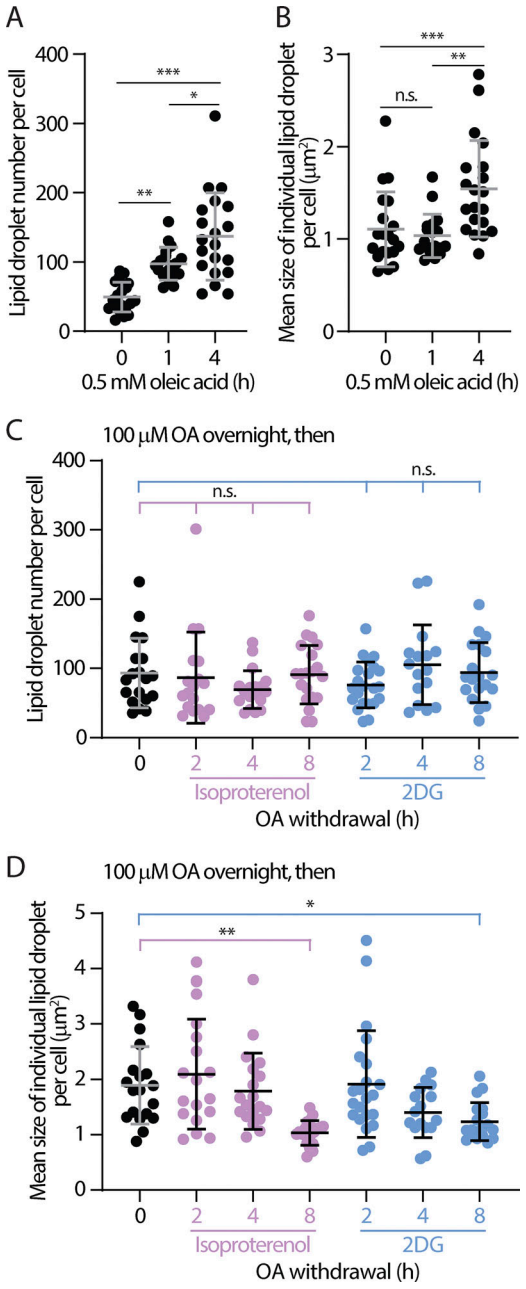

Figure S3. **Number and size of LDs following oleic acid (OA) addition and withdrawal. (A and B)** Quantification of lipid droplet (LD) number (A) and size (B) in HeLa cells pulsed with 500 µM of OA over time. Raw data and mean ± SD are shown (18–20 cells from three independent experiments). *P ≤ 0.05, **P ≤ 0.01, ***P ≤ 0.001, assessed by one-way ANOVA and Tukey's multiple comparisons test. **(C and D)** Number (C) and size (D) of LDs in OA-treated HeLa cells following OA withdrawal in DMEM and in DMEM with 10 µM of isoproterenol or 4 mM 2DG. Mean ± SD is shown (16–22 cells from three independent experiments). Statistical significance was compared to time zero. n.s. = not significant, *P ≤ 0.05, **P ≤ 0.01, assessed by one-way ANOVA and Tukey's multiple comparisons test.

Provided online are Table S1 and Table S2. Table S1 shows organelle targeting motifs. Table S2 shows oligonucleotides used in this study.